Department of Physics and Astronomy

University of Heidelberg

Master thesis

in Physics

submitted by

Jan Kilinc

born in Pforzheim (Germany)

March 2019

Starting a Na-K experiment for simulating quantum many-body phenomena

This Master thesis has been carried out by Jan Kilinc

at the

Kirchhoff Institute for Physics

under the supervision of

Prof. Dr. Fred Jendrzejewski

ABSTRACT

This thesis describes the construction of a new apparatus to study quantum gas mixtures of sodium and potassium. Our experimental approach entails, using two independent two-dimensional magneto-optical traps (2D MOTs) as sources of cold atoms for a dual-species magneto optical trap (3D MOT).

Therefore, we have implemented a versatile laser system, with which we are able to cool ^{39}K, ^{40}K and ^{23}Na. The laser light, which is stabilized to a spectroscopy line, is amplified with a home-built tapered amplifier, split and finally frequency-shifted to generate the cooler, repumper, Zeeman slower and push beam. We are able to switch between the two potassium isotopes using a beat lock system. To trap the atoms, we create magnetic quadrupole fields, employing permanent magnets in the 2D MOTs and magnetic field coils in the 3D MOT. Finally, I report on the implementation of a computer-based control system, which automatizes experimental sequences and simplifies parameter optimization processes.

Due to its tunability and flexibility, the new Na-K experiment will serve as a platform to study quantum many-body physics ranging from quantum thermodynamics to the investigation of lattice gauge theories.

ZUSAMMENFASSUNG

In dieser Arbeit wird der Aufbau eines neuartigen Experiments zur Untersuchung von ultrakalten Gasgemischen aus Natrium- und Kaliumatomen beschrieben. Unser Versuchsaufbau besteht aus zwei unabhängigen zweidimensionalen magneto-optischen Fallen (2D MOTs), welche als Quellen kalter Atome für eine gemeinsame magneto optische Falle (3D MOT) von Natrium und Kalium dienen.

Im Verlauf der Arbeit wurde ein flexibles Lasersystem installiert, welches uns die individuelle Kühlung von ^{39}K, ^{40}K und ^{23}Na ermöglicht. Das Laserlicht, welches mit Hilfe einer Spektrosokopie-Anordnung stabilisiert wird, wird zunächst verstärkt, dann aufgespalten und schließlich in der Frequenz verschoben. Wir nutzen einen Frequenzabstandslock, um zwischen den beiden Kalium-Isotopen zu wechseln. Um die Atome einzufangen, erzeugen wir des Weiteren Quadrupol-Magnetfelder, indem wir Permanentmagneten für die beiden 2D MOTs und Magnetfeldspulen für die 3D MOT verwenden. Schließlich, berichten wir von der Implementierung einer Computer-Steuerung, welche die Versuchssequenzen automatisiert und die Parameter-Optimierungsprozesse vereinfacht.

Aufgrund seiner Vielseitigkeit und Variabilität, wird das neue NaK-Experiment als Plattform für die Untersuchung der Quanten-Vielteilchenphysik dienen, die von der Quanten-Thermodynamik bis zur Untersuchung von Gittereichtheorien reicht.

CONTENTS

1 INTRODUCTION 1

2 COOLING AND TRAPPING ATOMS WITH LIGHT 5
- 2.1 Atom Light Interaction 5
- 2.2 Doppler Cooling and Optical Molasses 6
- 2.3 Magneto Optical Trapping 7
- 2.4 Summary 8

3 VACUUM SYSTEM 9
- 3.1 Chamber geometry 9
- 3.2 Pumping sequence 13
- 3.3 Summary 15

4 SPECTROSCOPIC TECHNIQUES 17
- 4.1 Atomic properties 17
- 4.2 Saturated Absorption Spectroscopy 19
- 4.3 Zeeman modulation locking 22
- 4.4 Summary 24

5 LASER SYSTEM 25
- 5.1 Potassium laser table 25
  - 5.1.1 Light generation 26
  - 5.1.2 Frequency offset lock 27
  - 5.1.3 Light amplification 29
  - 5.1.4 Frequency Shifting 32
- 5.2 Sodium laser table 37
- 5.3 Summary 39

6 IMPLEMENTATION OF THE 2D MAGNETO-OPTICAL TRAPS 41
- 6.1 Optics 41
- 6.2 Magnetic fields 42
- 6.3 Fluorescence 45
- 6.4 Summary 46

7 DUAL-SPECIES MAGNETO-OPTICAL TRAP 47
- 7.1 Optics 47
- 7.2 Magnetic coils configuration 48
- 7.3 Hunt for the K-MOT 51
- 7.4 Summary 52

8 EXPERIMENTAL CONTROL SYSTEM 53
- 8.1 Hardware 54
- 8.2 The labscript suite 56
- 8.3 Summary 57

9 CONCLUSION AND OUTLOOK 59

A TEMPERATURE CONTROL CIRCUIT 61

B ENERGY LEVEL SCHEMES 63

List of Figures 67

List of Tables 69

Bibliography 71

ACRONYMS

UHV	Ultra-High Vacuum
CF	ConFlat
HV	High Vacuum
MOT	Magneto-Optical Trap
RGA	Residual Gas Analyser
SAS	Saturated Absorption Spectroscopy
FMS	Frequency Modulation Spectroscopy
PBS	Polarizing Beam Splitter
ECDL	External Cavity Diode Laser
AOM	Acousto-Optical Modulator
EOM	Electro-Optical Modulator
VCO	Voltage-Controlled Oscillator
TA	Tapered Amplifier
ASE	Amplified Spontaneous Emission
SHG	Second-Harmonic Generation
GUI	Graphical User Interface
PFI	Programmable Function Input
NI	National Instruments
HDF	Hierarchical Data Format

1 INTRODUCTION

The primary motivation for the development of laser cooling techniques in the 1980s [1, 2], besides improving the performance of atomic clocks and increasing precision for spectroscopic purposes, was basic curiosity. With further advances in cooling methods and trapping schemes, temperatures in the range of nano-kelvin were soon reached. At these ultra-low temperatures we enter the quantum regime, where it now matters if the atoms are bosons or fermions. Fermions form a degenerate Fermi gas [3, 4], which is similar to electrons in metals. On the other hand, bosons undergo a phase transition to a new state of matter known as a Bose-Einstein condensate [5, 6].

Considering the precise control over experimental parameters, such as temperature, dimensionality, geometry or interaction strength, these ultracold quantum systems enable the simulation of complicated physical processes in nature [7, 8]. Within this approach, we take a complex system that is hard to manipulate and not straightforward to study and simulate it with another quantum system, which is governed by the same equations but is tunable and well-controlled.

Ultracold atomic mixtures extend the large range of applications even further. Adding a second atomic species, offers a versatile experimental platform to study strongly interacting many-body phenomena such as:

QUANTUM THERMODYNAMICS Due to inter-species interactions, a bosonic species, such as ^{23}Na, can be used as a sympathetic coolant for a fermionic species [9, 10]. This is particularly useful for atomic species that cannot be cooled efficiently with optical methods.

Another exciting new approach in the field of quantum thermodynamics is the concept of cooling atomic clouds with the quantum analogue of a refrigerator [11]. Within this scheme, tightly confined clouds of K-atoms are moved between two (hot and cold) baths of sodium atoms (see figure 1.1). The potassium atoms act as a working

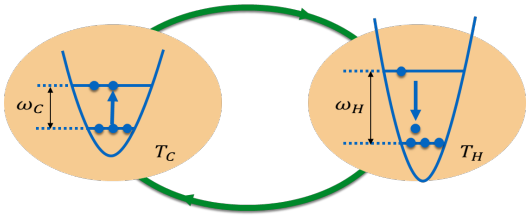

Figure 1.1: Schematic representation of the quantum heat engine. The working medium (blue atoms) is transferred between two baths of sodium atoms (orange clouds).

fluid and transfer energy from the cold to the hot bath, thereby cooling one of the sodium clouds below condensation threshold over the course of many cycles. The work input, necessary for refrigeration, is supplied by an external laser, that varies the energy level spacing of the working fluid during the transfer.

HIGH ENERGY PHYSICS Gauge fields lie at the core of the standard model of particle physics as they mediate the strong and electro-weak forces between matter. As experimental and theoretical techniques struggle when dealing with the complex many-body dynamics of gauge fields, quantum simulations offer a new pathway.

One route of implementing lattice gauge theories lies in using a Bose-Fermi mixture in an optical lattice, which is illustrated in figure 1.2. The lattice potential is attractive (repulsive) for the fermions (bosons), such that the two species are spatially separated. The gauge-invariant interactions are implemented using boson-fermion spin-changing collisions [12].

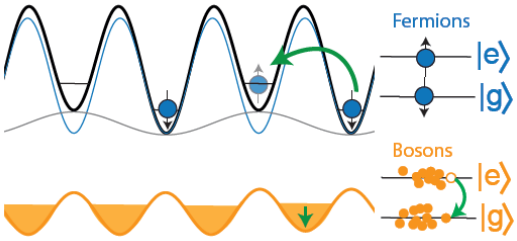

Figure 1.2: Schematic illustration of the experimental implementation of dynamical gauge fields with ultracold atoms. The fermionic species (blue) takes the role of the matter field, while the bosonic sodium atoms (orange) realize the gauge field [12, 13].

CONDENSED MATTER PHYSICS The Kondo effect describes the peculiar temperature dependence of the electric conductivity due to the interaction of magnetic impurities with non-interacting electrons in a metal [14].

In an ultracold atomic mixture experiment, a small number of atoms of one species (e.g. ^{23}Na) could act as an impurity immersed in a large Fermi sea formed by the other species (e.g. ^{40}K). A schematic representation is shown in figure 1.3. The tight confinement of the impurity

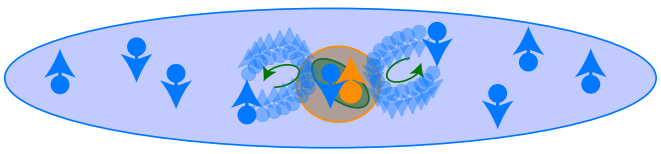

Figure 1.3: A Fermi sea of ^{40}K-atoms (blue) is coupled to a tightly confined, localized ^{23}Na-impurity (orange) [15]. In the vicinity of the Kondo temperature the magnetic impurity can mediate interactions between the otherwise non-interacting fermions.

can be achieved by species-selective optical potentials, whereas the spin-exchange could be mediated by spin-changing collisions [15].

WHY SODIUM AND POTASSIUM?

Both atomic species have been investigated extensively over the last decade. The wealth of literature [16–21] simplifies the experimental implementation and provides a certain robustness to the experiment.

Moreover, the different natural isotopes of potassium (^{39}K and ^{40}K) offer the ability to switch between Boson-Boson and Boson-Fermion mixtures. This expands the scope of possible physical systems one is able to simulate, as seen in the previous three application examples.

Furthermore, ^{23}Na-^{39}K and ^{23}Na-^{40}K mixtures possess moderately wide inter-species Feshbach resonances at low magnetic fields less than 300 G [20–22], easing the experimental implementation.

THESIS OVERVIEW

This manuscript details the setup of a new Na-K mixture experiment, which we started to construct in the course of this thesis. Based on our knowledge with the existing Na-Li experiment, we aimed at setting up a more compact, modular and versatile machine for exploring strongly coupled many-body systems.

The manuscript is structured in the following way:

- Chapter 2 introduces the theoretical principles of laser cooling and trapping. From the origin of the scattering force to the principles of a Magneto-Optical Trap (MOT), it covers the necessary theoretical prerequisites for the experimental part.
- Chapter 3 describes the geometry of the vacuum apparatus. After studying the designs of the different chambers, we list the steps it takes obtain an ultra-high vacuum utilizing different pumps.
- Chapter 4 is dedicated to the spectroscopic techniques, which were used to stabilize the frequency of the lasers.
- Chapter 5 presents a detailed description of the laser system. This includes the two laser tables, where the focus is kept on the generation of cooling and trapping light for potassium.
- Chapter 6 outlines the layout of the two-dimensional magneto-optical traps in terms of necessary optics and magnetic fields.
- Chapter 7 shows the implementation of the dual-species three-dimensional trap. We provide an overview of the different magnetic field coils surrounding the science chamber and further describe some problems we faced when trying to achieve a MOT of potassium.
- Chapter 8 finally introduces the experimental control system, enabling the precise timing of experimental sequences. We discuss

the features of the different hardware devices and how these devices can be interfaced with the software program *Labscript suite*.

2

COOLING AND TRAPPING ATOMS WITH LIGHT

At room temperature atoms fly around approximately at the speed of sound. However, in order to study and manipulate these atoms, they need to be slowed down or even trapped. Once they have been slowed down sufficiently, we can determine their properties much more precisely.

In the following sections I will give a brief theoretical introduction into laser cooling and trapping of neutral particles. After discussing the interaction between atoms and photons, which lead to the cooling force, I will present how an atomic beam can be slowed down. Combining the techniques of laser cooling with magnetic field gradients can be used to trap neutral atoms, which will be described in the final section. A more detailed description of the underlying principles of laser cooling and trapping can be found in [23, 24].

2.1 ATOM LIGHT INTERACTION

Let's consider the interaction of an atom, described by a two-level system with an excited state $|e\rangle$ and a ground state $|g\rangle$, with a photon with momentum $\mathbf{k} = k\,\mathbf{e}_x$. The ground-state atom can absorb the photon, receiving a momentum kick $\mathbf{k}$ in the direction of photon propagation ($+x$-direction). The excited atom has two ways of relaxing to its ground state; either via stimulated or spontaneous emission.

In the case of stimulated emission, the atom emits a photon in the travel direction of the absorbed photon, resulting in no net momentum change. As spontaneous emission is an isotropic process, the direction of the emitted photon is random. Consequently, multiple cycles of absorption and spontaneous emission lead to a net force in direction of light propagation, which is referred to as the scattering or dissipative force and has the following form:

Scattering force

$$\mathbf{F}_{\text{scatt}} = \hbar\mathbf{k}\,\frac{\Gamma}{2}\,\frac{I/I_{\text{sat}}}{1 + I/I_{\text{sat}} + 4\,\delta^2/\Gamma^2} \tag{2.1}$$

using the relation $I/I_{\text{sat}} = 2\,\Omega^2/\Gamma^2$, where

- $\mathbf{k}$ momentum of photon
- Γ spontaneous emission rate
- δ detuning
- Ω Rabi frequency

At high intensities the scattering force saturates to a limiting value $\mathbf{F}_{\text{scatt, max}} = \frac{\hbar\,\mathbf{k}\,\Gamma}{2}$, indicating that the average population of the excited state approaches $1/2$.

2.2 DOPPLER COOLING AND OPTICAL MOLASSES

Now imagine a situation, where an atom travels with velocity v inside a light field created by two red-detuned counter-propagating laser beams. For $v = 0$, there is no resultant force, since the scattering is the same for both beams. However, if the atom moves in the direction of one of the beams (i.e. $v \neq 0$), the Doppler effect shifts the atom into resonance with the counter-propagating beam, resulting in an imbalance of forces (see figure 2.1a).

The resultant velocity-dependent force, which is plotted in figure 2.1b, has the form:

$$\begin{aligned} \mathbf{F}_{\text{scatt}} &= \mathbf{F}_+ - \mathbf{F}_- \\ &= \mathbf{F}(\delta - kv) - \mathbf{F}(\delta + kv) \\ &\approx -\alpha\, v \end{aligned} \tag{2.2}$$

with the damping coefficient $\alpha = 2\,k\,\frac{\partial F}{\partial \omega}$. The approximation in equation 2.2 is only valid at low velocities, where $|\mathbf{k}\,\mathbf{v}| \ll \Gamma$ holds true. To guarantee the damping character of the scattering force, α has to be positive, which means that the laser has to be red-detuned ($\delta < 0$).

As the net force always opposes the velocity, the atoms are slowed down no matter in which direction they travel. This method is known as Doppler cooling. The random velocity changes, caused by spontaneous emission of photons, lead to heating of the atoms, that sets the limit in terms of temperature (Doppler temperature):

Doppler limit

$$T_{\text{Doppler}} = \frac{\hbar\,\Gamma}{2\,k_B} \tag{2.3}$$

where k_B is the Boltzmann constant.

Up until now, we restricted the discussion to one dimension, where two counter-propagating laser beams are employed. This scheme can

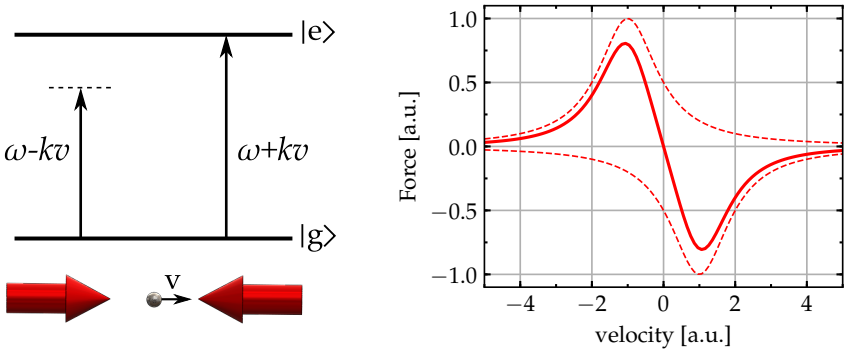

(a) 1D Doppler cooling scheme. The atom with states $|g\rangle$ and $|e\rangle$ travels with velocity v.

(b) Velocity dependence of the scattering force. The contributions from the two counter-propagating beams, marked by the dashed curves, add up to the total force (solid line).

Figure 2.1: Doppler cooling configuration with the resulting velocity dependent scattering force.

easily be extended to higher dimensions by adding a pair of counter-propagating laser beams for each spatial direction. Finally, we end up with a configuration of six laser beams, which all intersect at one single point, where the atoms are finally cooled. This technique is called optical molasses.

2.3 MAGNETO OPTICAL TRAPPING

However, the atoms, even though they are slowed down, are not trapped through the optical molasses technique, as the scattering force only confines them in momentum space. Therefore, the atoms can perform a random walk and leave the cooling area. This problem can be overcome in a Magneto-Optical Trap (MOT) by adding a magnetic field gradient, leading to a spatially-dependent force.

The magnetic field gradient is supplied by a pair of coils in anti-Helmholtz configuration, i.e. current is running through the coils in opposite directions. This creates a quadruple field with a linear field gradient where the six circularly polarised molasses beams intersect, and where the atoms are trapped (see figure 2.2a).

The principle behind combining magnetic fields and light to trap atoms is schematically illustrated in figure 2.2b, reducing the problem to one dimension.

Let's consider the atomic transition $J = 0 \rightarrow J' = 1$, where the excited state has a three-fold $m_{J'}$-manifold due to the presence of a magnetic field. The shift of the $m_{J'} = \pm 1$ states, according to the linear Zeeman-effect, is linearly proportional to the magnetic field. Because of the uniform magnetic field gradient along the z-axis, the energy shift maps onto the z-position.

Looking at figure 2.2b, we have an atom in the centre at $B = 0$, a σ^+ polarised beam in +z-direction and a counter-propagating σ^- beam. Both beams are red-detuned with respect to the atomic transition, so that they do not interact with the atom at $z = 0$. If the atom moves

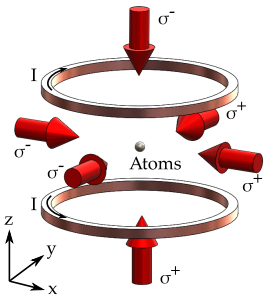

(a) 3D drawing of the MOT configuration with the trapped atoms in the centre.

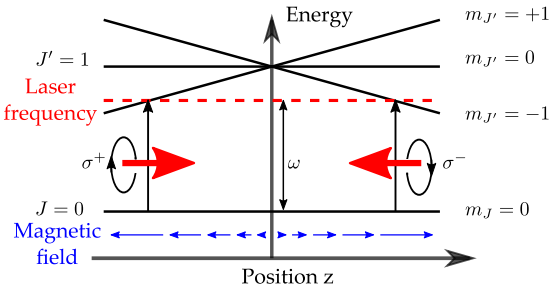

(b) Working principle of a 1D MOT with its linear magnetic field gradient along z. The frequency of the cooling light is denoted by ω.

Figure 2.2: MOT setup and energy diagram illustrating the working principle in one dimension.

in +z-direction it comes into resonance with the σ^- light. The same applies to the -z-direction, where the atom would absorb σ^+ light. Due to the selection rules, each pair of counter-propagating laser beams has to have opposite polarisation for the scheme to work.

For a magnetic field gradient along x-, y- and z-direction and with six laser beams as sketched in figure 2.2a, there is a harmonic confinement adding to the velocity-dependent scattering force that cools the atoms.

2.4 SUMMARY

Originating from the process of spontaneous emission, the scattering force dampens the atoms motion with the help of red-detuned counter-propagating light. To trap and efficiently cool neutral atoms, we employ a magneto-optical trap combining:

- A pair of red-detuned counter-propagating laser beams with opposite circular polarization along each spatial direction.
- Magnetic field gradients along the beam paths.

As the MOT constitutes the first stage of trapping, it lies at the heart of every ultracold atom experiment.

3

VACUUM SYSTEM

At atmospheric pressure (1 bar) atoms perform a random movement with thermal velocities. In the proposed experiments, we would like to cool down the atomic sample to temperatures of the order of a few nK. Due to collisions and the associated transfer of kinetic energy, the cold atoms heat up.[1] To reduce the amount of collisions we have to create an Ultra-High Vacuum (UHV) with a pressure less than 10^{-11} mbar.

When designing a vacuum system, the following aspects have to be kept in mind:

- The different chambers should have good optical access for the various cooling and trapping laser beams. Considering the sizes of the beams, the viewports have to be chosen in accordance.
- All vacuum components should be made out of material with a low out-gassing rate (i.e. desorption of gases from the surface of vacuum components). The two most popular choices are stainless steel or titanium.
- The material should be non-magnetic, since the atoms inside the chamber are sensitive to magnetic fields. The same applies to all kinds of screws and washers within the setup. We chose titanium rather than steel for the vacuum chambers, because it is as strong as steel, but less magnetic and about 50% lighter.
- To achieve a UHV, the standard technique is to connect vacuum components by two ConFlat (CF) flanges with a copper gasket in between. The knife edges from the two flanges cut into the relatively soft gasket, sealing this connection.

This chapter provides a description of the main features of the vacuum system. After introducing the different chambers of the experiment, we will go through the sequence of steps needed for pumping down the chambers.

3.1 CHAMBER GEOMETRY

The vacuum system, which is illustrated in figure 3.1, can be divided into two sections. These regions can be classified by the pressure inside:

1 In 2017 a research group at the National Institute of Standards and Technology (NIST) began to develop an absolute pressure sensor employing ultracold atoms themselves [25]. They utilize losses from a magneto-optical trap due to collisions with background gas molecules as a means to gauge the pressure inside the chamber.

- A High Vacuum (HV) section, which includes the two-dimensional MOTs for sodium and potassium. The two chambers are completely identical in their design. Here, the thermal atoms from the oven are initially slowed down. During operation (i.e. oven is heated), the pressure is of the order of 10^{-8} mbar.
- A UHV region, where atoms are further cooled, trapped and manipulated at pressure readings below 10^{-11} mbar. This region is composed of the main chamber and the science chamber, where the atoms are trapped in a three-dimensional MOT. The angle of the two bellows with respect to the main chamber has been chosen such that the two atomic beams cross exactly in the centre of the science chamber.

To maintain this pressure gradient between the two sections, a differential pumping stage is placed directly behind each 2D MOT.

In the design of the vacuum apparatus, which is mounted on a 1.5 m x 2.4 m x 305 mm optical table (*Newport* M-RPR-58-12), we tried to optimize two features: modularity and compactness. The modular setup was achieved by evacuating different chambers from each other

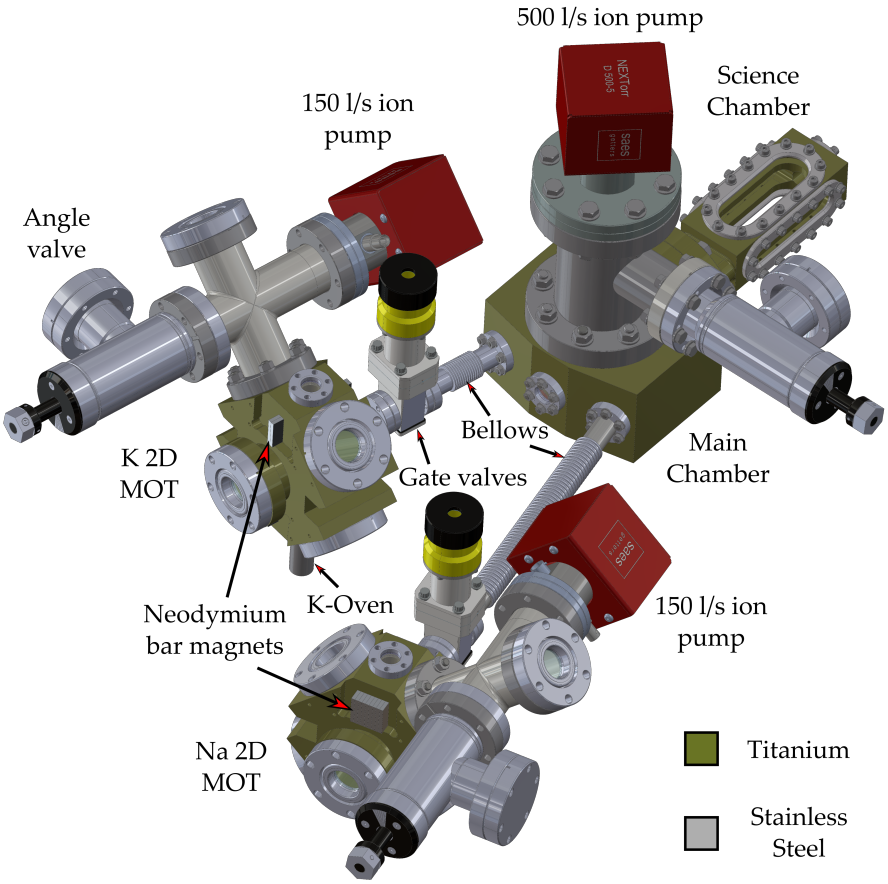

Figure 3.1: 3D view of the entire vacuum system. The K and Na 2D MOTs are accomplished in two separate chambers. The atoms are then transferred through a gate valve, a bellow and the main chamber into the science chamber. In the science chamber, where, we maintain an UHV below 10^{-11} mbar, they are recaptured in a 3D MOT.

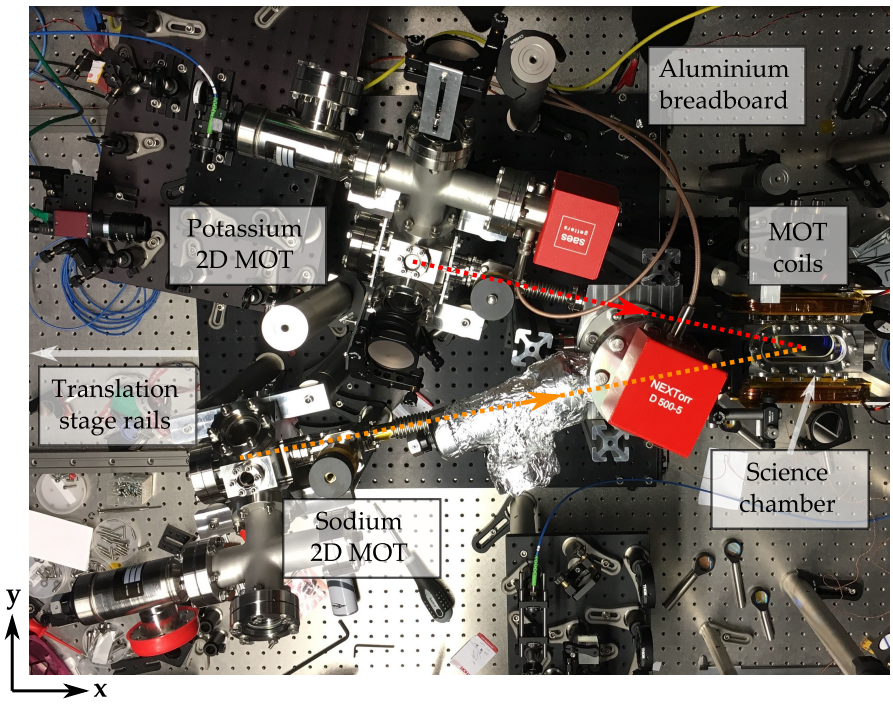

Figure 3.2: Picture of the assembled vacuum apparatus from a bird's-eye view. The dotted lines indicate the transfer of sodium (orange) and potassium (red) atoms from the 2D-MOT to the science chamber, where they are recaptured in a dual-species MOT. The whole system is mounted on a translation stage, which can be moved along the x-direction (coordinate system in the bottom left hand corner).

with the help of gate valves. This way the potassium 2D MOT, the main and science chamber, and the sodium 2D MOT can be pumped down individually. Moreover, if there is a leak in one chamber, we can close the valve and the rest of the system is not affected. Secondly, with a total length of approximately 80 cm, the whole system is very compact[2] in comparison to our previous generation Na-Li apparatus that spans over 250 cm. We chose this size as a trade-off between compactness on the one side, and robustness and modularity on the other side.

Translation stage

Furthermore, inspired by the group of Manual Endres at the California Institute of Technology [27], the entire apparatus is mounted on a 600 mm x 700 mm aluminium breadboard, which is fixed onto a linear translation stage (*Igus* TS-01-25 and TW-01-HKA), as shown in figure 3.2. The entire vacuum system can, therefore, be moved along the x-axis, indicated by the white arrow, over a distance of 42 cm. This makes it possible to bake the system without disturbing the surrounding optics. Additionally, it was extremely helpful during the alignment of the 3D MOT beams.

Geometry of 2D MOT chambers

The octagonal 2D MOT chambers, manifactured by *SAES* and displayed in figure 3.3a, each have four CF40 viewports on the diagonal

2 There are also research groups miniaturizing cold-atom experiments utilizing e.g. a nano-fabricated diffraction grating to generate a magneto-optical trap [26].

sides, where the circularly-polarized MOT beams enter, and one CF40 viewport on the front, where the push beam enters. The chamber is supported by four Ø1.5 inch aluminium rods, which are fixed to the chamber via two rectangular aluminium pieces. The design and setup of the 2D MOTs is inspired by the work of the group of Gabriele Ferrari in Trento [28].

The oven, which contains the atomic ampoule and has a diameter of 16 mm, is connected from below via a CF16 flange. Furthermore, there is a CF16 viewport on top of the chamber, where a Zeeman slowing beam enters.

The windows are made from fused silica with a broadband anti-reflection coating. The chamber has four rectangular recesses on the outside, where Neodymium bar magnets (ECLIPSE N750-RB) are inserted. These recesses are located on the front and the back of the chamber above and below the viewport. The top slot on the front can be seen in figure 3.3a. The magnets are fixed to the chamber in the centre position with aluminium plates, which are screwed to the sides of the chamber. More details on the placement and importance of these magnets will be discussed in section 6.2.

Both 2D MOTs are connected to an ion pump via a T-piece. The other ends of the T's are attached to all-metal angle valves (*MDC* MAV-150-V), where the pre-pumping station can be connected. This station consists of a roughing pump, a turbo-molecular pump and a Residual Gas Analyser (RGA).

Main and science chamber

The two 2D MOTs are connected to the main chamber with two CF16 bellows of different sizes. The one on the potassium side is 76.2 mm long and the sodium bellow is 254 mm long. This ensures that there is enough space for the 2D MOT optics and the chambers themselves.

The main chamber serves two purposes: it assists as a connection piece between the two bellows and the science chamber, and it connects to an ion pump, which creates the UHV in the science chamber. The pump is mounted on top of the chamber via a CF63 flange.

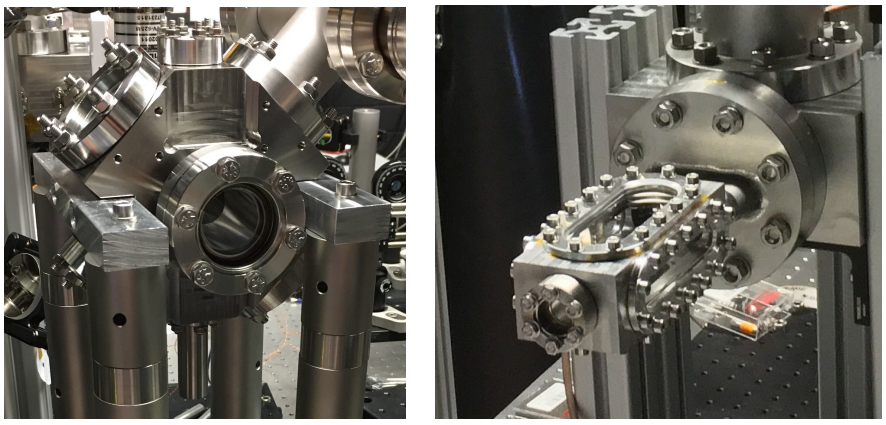

(a) Side view of the 2D MOT chamber. (b) Rectangular science chamber.

Figure 3.3: Images of the vacuum chambers on the main experimental table.

The rectangular science chamber (see figure 3.3b) has four elongated oval viewports. This shape maximizes the optical access for the different laser beams and allows for a high resolution imaging system. Because there are no gaskets with this specific pattern, these flanges are sealed with flexible indium wire. The wire is placed into the notch of the chamber, the window is inserted and then the flange is screwed-in evenly. Between the window and the flange, we added a layer of Teflon to protect the glass.

3.2 PUMPING SEQUENCE

The process of pumping down the vacuum system has to be done stepwise, because each pump has its own limited operational range:

1. First of all, we connect the pre-pumping station (roughing pump, turbo pump and RGA) to one of the three all-metal angle valves.
2. We open the valve and start the roughing pump. In this oil-sealed rotary vane pump, the gas gets compressed and then forced towards the exhaust by a turning rotor reaching a pressure of approximately 10^{-3} mbar.
3. Once a pressure of 10^{-3} mbar has been reached, we turn on the turbo-molecular pump. Similar to a jet turbine, a series of rotors turn at 20.000 to 90.000 rpm [29]. Due to the canted rotor blades the gas molecules are dragged towards the exhaust providing a vacuum of the order of 10^{-8} mbar.
4. The last part of the pre-pumping station is the RGA, which is used to detect possible leaks by measuring the partial pressures of the residual gases.
5. `Baking:` To further lower the pressure inside the chamber, one should perform a bake-out. In this process the entire vacuum system is heated up very slowly and homogeneously, to avoid any damage to the windows. The heating releases unwanted residual substances such as water molecules from the inner walls of the chamber, which are then pumped out by the turbo pump. The homogeneous heating can be achieved by putting a layer of aluminium foil around the chamber and then wrapping glass fibre-insulated heating tape (Isoheat MiL-HT-BS30) around it. During the bake-out we monitored the temperature at various positions using K-type thermocouples.
6. `Ion pump:` An ion pump combines getter pumping with pumping via an ionization gauge [29]. Residual atoms or molecules will get ionised and accelerated towards the cathode in a 5 kV electric field, where they get chemically bound. Active gases will get bound without previous ionization when they hit the titanium getter material (chemisorption). The residual gas is not pumped out of the vacuum, but rather buried on the surface of the pump. Turning on the ion pump requires the following steps:

a) First we flash the ion pump by switching it on and off a few times. This will release unwanted particles from the pump's surface, which can then be pumped out by the turbo pump.

b) To activate the getter element's pumping characteristics, the material is heated to about 550 °C under vacuum for 60 minutes.

c) Lastly, we turn on the ion pump again. Since the current drawn is proportional to the pressure inside the chamber, these pumps also act as a pressure gauge.

In total there are three ion pumps, which equates to one for each vacuum section. For the 2D MOTs we have two NEXTorr Z100 pumps (SAES). These pumps have a pumping speed of up to 150 l/s. On the other hand, the UHV in the science and main chamber is produced by a single NEXTorr D500-5 pump (SAES) featuring pumping speeds in excess of 500 l/s.

Characterization of the differential pumping stage

As mentioned in the previous section, a differential pumping stage is used to uphold the pressure gradient between the HV- and the UHV-region [30]. The front view and a 3D section view are shown in figure 3.4. The tube, which can be identified as the black spot in the middle of figure 3.4a, has a length of $l = 3$ cm and a diameter of $d = 3$ mm, enabling a conductance of:

$$C_{\text{diff}} = 12.1\frac{d^3}{l} \approx 0.11 \text{ l/s} \tag{3.1}$$

With a pumping speed of $S_P = 500$ l/s in the UHV-section, one gets:

$$\frac{P_{\text{UHV}}}{P_{\text{HV}}} = \frac{C_{\text{diff}}}{S_P} \approx 2.2 \times 10^{-4} \tag{3.2}$$

Due to the geometry of the differential pumping stage, the pressure in the 2D MOT chamber can be $\sim 10^4$ times higher than in the science chamber, where we want to maintain a UHV at 10^{-12} mbar.

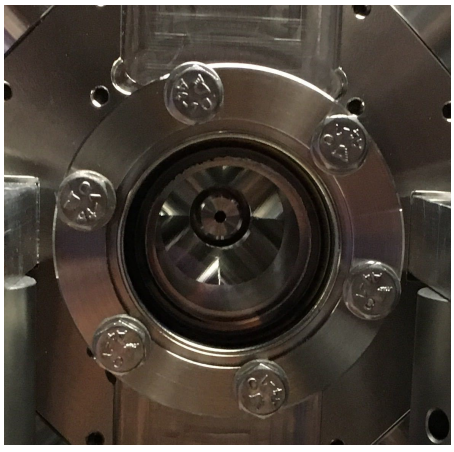

(a) Front view of the 2D MOT chamber looking through the push beam viewport.

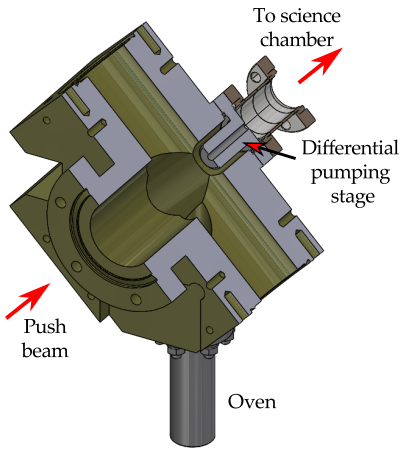

(b) Section view of the 2D MOT with its differential pumping stage. The cut is at a 45° angle wrt. the oven.

Figure 3.4: Differential pumping stage between the 2D MOT and the main chamber.

3.3 SUMMARY

The vacuum system consists of a HV-section (10^{-8} mbar) and a UHV-region, where the pressure can be lowered down to 10^{-12} mbar, reducing collisions with residual particles.
The HV-part features two independent two-dimensional MOT-chambers, one for sodium and the other for potassium. The pre-cooled atoms from each 2D-MOT are transferred through a differential pumping stage into the science chamber. Here, they are recaptured in a dual-species three-dimensional magneto-optical trap.

4

SPECTROSCOPIC TECHNIQUES

Cooling and trapping atoms requires laser control at the level of the linewidth. We are working with laser light at frequencies of several hundred THz, but require a stability and precision to within 5 MHz, which seems like an impossible task.

However, we can exploit the atoms themselves, by using them as a reference in a spectroscopy scheme. Locking the laser to an absorption feature, stabilizes its frequency output and most importantly tunes the laser to the correct absolute frequency.

In the course of this chapter we will go through the steps it takes to stabilize the frequency of a diode laser. As we want to lock the laser to an atomic resonance, we will firstly review the most important atomic properties, such as isotope composition and energy level structure, of potassium and sodium. Next, we will show how to obtain the spectrum using Saturated Absorption Spectroscopy (SAS), and lastly how we manipulate it in order to extract an error signal, which can be used to lock the laser.

4.1 ATOMIC PROPERTIES

Table 4.1 summarizes the properties of the three natural potassium isotopes and the only stable sodium isotope. The isotopes of interest in this experiment are the bosonic species ^{39}K and ^{23}Na and the far less abundant fermionic isotope ^{40}K. In the case of potassium, ^{39}K is used for spectroscopy, as it is more abundant and thus provides the stronger signal.

Vapour pressure

Another important characteristic when dealing with a spectroscopy cell is the vapour pressure. If the vapour pressure is too low, the absorption rate is not high enough and the spectroscopy signal cannot be resolved. Figure 4.1 displays the temperature dependence of the vapour pressure of potassium and sodium. At room temperature the

Table 4.1: Properties of natural potassium and sodium isotopes. Data taken from [31].

	ABUNDANCE [%]	LIFETIME	I*	
^{39}K	93.2581(44)	stable	3/2	bosonic
^{40}K	0.0117(1)	1.28×10^9 y	4	fermionic
^{41}K	6.7302(44)	stable	3/2	bosonic
^{23}Na	100	stable	3/2	bosonic

*Nuclear spin

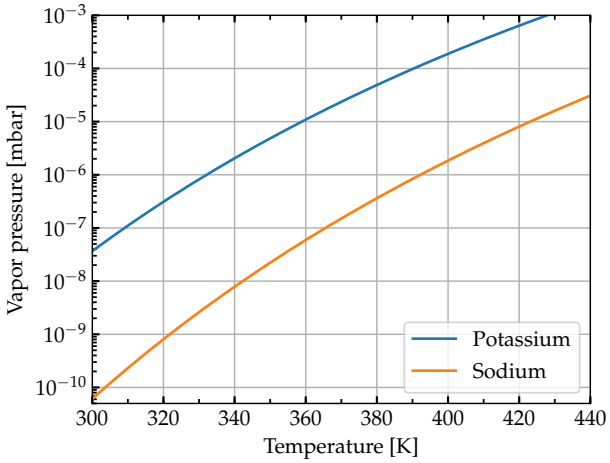

Figure 4.1: Vapour pressure of potassium and sodium as a function of temperature. Data taken from [32].

vapour pressure of potassium is of the order of 10^{-8} mbar, whereas it is at $\sim 10^{-11}$ mbar for sodium. However, as the temperature increases, the pressure rises. In order to get a strong absorption signal, one has to heat the spectroscopy cell, filled with either potassium or sodium, to higher temperatures.

For our potassium spectroscopy cell, we observed the strongest signal for a temperature of 70 °C, whereas we had to heat the sodium cell up to 130 °C.

To understand the spectra of the different atomic species, we need to look at their respective energy level schemes, which are displayed in figure 4.2. The different states are represented in the form $n^{2S+1}L_J$ with the principal quantum number n. Both species have one valence electron, which fixes the total spin to $S = 1/2$.

Fine-structure

The coupling between spin $\vec{S}$ and orbital angular momentum $\vec{L}$ gives rise to the fine-structure splitting characterized by $\vec{J} = \vec{L} + \vec{S}$. The ground state has $L = 0$ (S-state), so that J has to be $1/2$. On the other

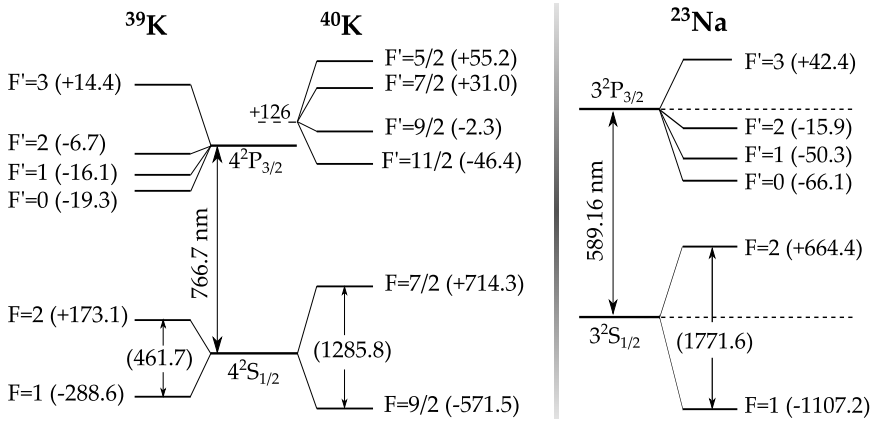

Figure 4.2: Energy level scheme for the D_2-line of ^{39}K, ^{40}K and ^{23}Na. The frequency shifts of the hyperfine levels are displayed in brackets in terms of MHz (figure is not to scale).

hand, the excited state (P-state) is split into $J = 1/2$ and $J = 3/2$. The $J = 1/2$ state has been omitted in figure 4.2, as it is not used in the spectroscopy.

Hyperfine-structure

Furthermore, the nucleus has a magnetic moment that is related to the nuclear spin I. The interaction between the nuclear magnetic moment and the magnetic field produced by the electrons leads to the hyperfine-splitting, which is quantized by $\vec{F} = \vec{I} + \vec{J}$. Because of the nucleus's large mass compared to the electron's, this energy separation is ~ 2000 times smaller than the fine-structure splitting.

4.2 SATURATED ABSORPTION SPECTROSCOPY

In the conventional spectroscopy scheme a resonant laser beam is sent through a gas-filled vapour cell and one observes the transmitted intensity. By tuning the frequency around the atomic resonance, a Doppler-broadened absorption feature appears. This is the result of the random thermal motion of the atoms at finite temperatures and the associated Doppler effect. As the moving atoms see the light red- or blue-shifted depending on their propagation direction, they absorb light that does not coincide with the atomic resonance, leading to a broadened absorption feature.

As $\Delta\omega_{\text{Doppler}} \gg \Delta\omega_{\text{nat}}$ (with Doppler width $\Delta\omega_{\text{Doppler}}$ and natural linewidth $\Delta\omega_{\text{nat}}$) we are spectroscopically limited by the Doppler broadening.

Theory of Saturated Absorption Spectroscopy (SAS)

The Saturated Absorption Spectroscopy (SAS) scheme can get rid of this broadening feature by using two counter-propagating laser beams. Coming from the same laser, the two beams have the same frequency, but should differ in intensity. If one beam interacts with atoms, which travel at velocity v, then the counter-propagating beam will excite atoms with a velocity of $-v$.

Only if both beams are on resonance, do they then affect the same class of atoms, namely those with velocity $v = 0$. In this case, the strong pump beam will excite many atoms, so that the transition is saturated. The weaker probe beam cannot be absorbed, causing the medium to appear transparent to the second beam, which leads to an absorption dip (transmission peak). As only atoms with a velocity of $v = 0$ are affected by this technique, this dip is purely limited by the natural linewidth.

Crossover resonances

The situation gets more complex if we have two transitions with frequencies ω_1 and ω_2 that share a common ground or excited state and whose energy separation is less than the Doppler width: $\omega_2 - \omega_1 < \Delta\nu_{\text{Doppler}}$. In this case a crossover resonance appears at $\frac{\omega_1+\omega_2}{2}$, since the non-zero velocity class, the two beams interact with, is the same.

The crossover resonance can be a dip or peak depending on whether the two transitions possess a shared ground or shared excited state. If they share one ground state (V-system), the pump beam saturates

these atoms, making the medium transparent for the probe beam. This leads to the appearance of a peak in the transmitted intensity.

On the other hand if there are two ground states and one shared excited state (Λ-system), one observes a dip as a result of optical pumping between the ground states. The pump beam depopulates the ω_1 transition, letting the probe beam excite the ω_2 ground state atoms. This effect causes an increased absorption rate, translating to a dip in transmission.

Temperature Control

As seen in figure 4.1, we need to heat the spectroscopy cells to get a strong absorption signal. Thus, the two ends of the spectroscopy cells are embedded in custom-made brass cylinders (see figure 4.3), which act as heat conductors and ensure that the cell is uniformly heated along these ends. By not heating the centre of the cell, we shift the coldest point to the middle, which prevents condensation of potassium or sodium on the outer windows. The heating is performed by two mineral insulated band heaters (*Watlow* MB1J1JN3-B12) with a diameter of 40 mm. In order to control the temperature of such a band heater, we adjust the current running through the element wire.

For the two species we have two different ways of achieving this:

- `Potassium thermistor circuit:` A thermistor close to the cell senses the actual temperature. This value is compared to a predefined setpoint and depending on the error, an Arduino UNO actuates the band heaters via a solid-state relay. This feedback mechanism minimizes temperature fluctuations down to ± 10 mK. The underlying electronic circuit can be found in Appendix A.

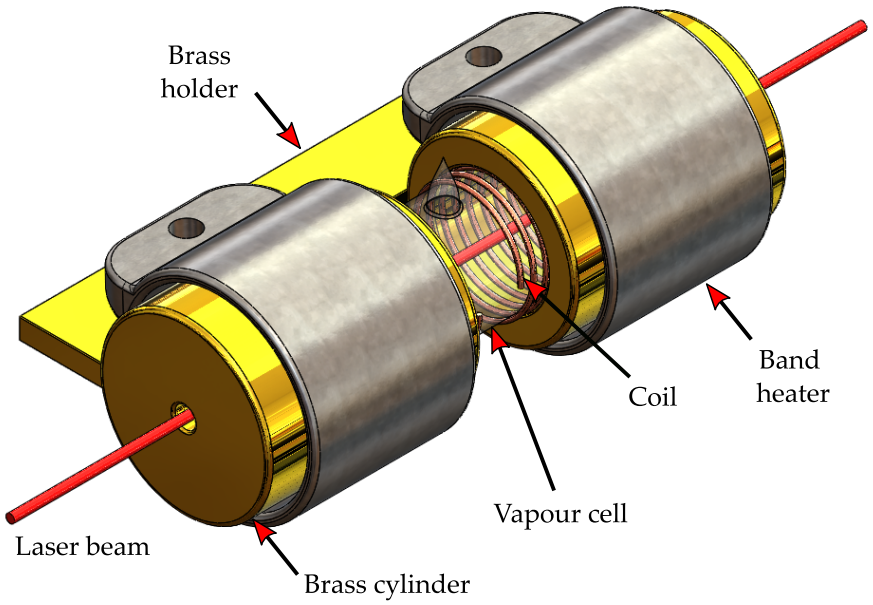

Figure 4.3: 3D view of the spectroscopy cell encased in two brass cylinders with two heating bands attached on the outside. The brass holder can be mounted to a post and then fixed to the optical table.

- `Sodium thermocouple circuit:` The temperature is measured by a K-type thermocouple, amplified by a MAX31855 breakout board and recorded by an Arduino UNO. The micro-controller then triggers a phase-angle dimmer (NS-80), which continuously regulates the current running through the heaters.

We started out with the thermistor circuit for potassium, which excelled due to its low cost and high stability. However, we came across a much simpler solution provided by the thermocouple circuit. As it features only a few components, it is inexpensive, and very easy and quick to assemble. Therefore, we also incorporated this circuit into the heating of the two ovens.

Optical setup

The SAS optical setup is shown in figure 4.4. As a laser source we use the fiberized output of a tunable diode laser (TOPTICA DL Pro) at a wavelength of 766.701 nm.

Using a half-wave plate ($\lambda/2$) we make sure that all the light goes through the Polarizing Beam Splitter (PBS) without any reflections. The most convenient way to achieve the pump-probe scheme is to let the beam pass through the vapour cell once and then reflect it on the other side by means of a dielectric mirror. This technique ensures that the two beams have the same frequency and an iris can lower the intensity of the probe beam.

A combination of a PBS and a quarter-wave plate deflects the light, which traversed the cell twice, onto a home-built photodiode. With this photodiode we monitor the Doppler-free absorption signal.

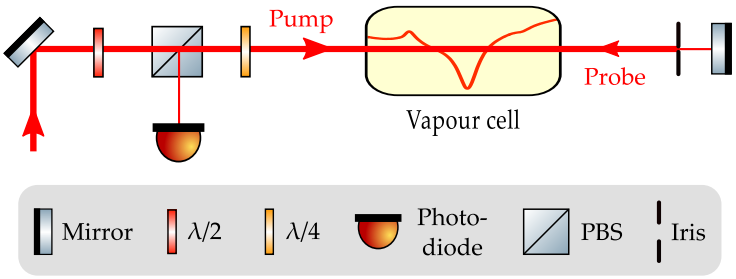

Figure 4.4: Optical layout for saturated absorption spectroscopy, with $\lambda/2$: half-wave plate, $\lambda/4$: quarter-wave plate, PBS: polarizing beam splitter.

SAS spectra

The spectra of potassium and sodium are displayed in figure 4.5. Since the energy level structure of the two atomic species is very similar, so are their spectra. The only major difference is the frequency separation of the different peaks, which is caused by the ground state energy splitting (see figure 4.2): 461.7 MHz for ^{39}K and 1771.6 MHz for ^{23}Na.

The three main features in both spectra are labelled and marked by grey dotted lines. Feature A corresponds to the transition F = 2 to F′ and feature B to F = 1 to F′. The most pronounced signal, which lies exactly between A and B, is the crossover transition. As we are dealing

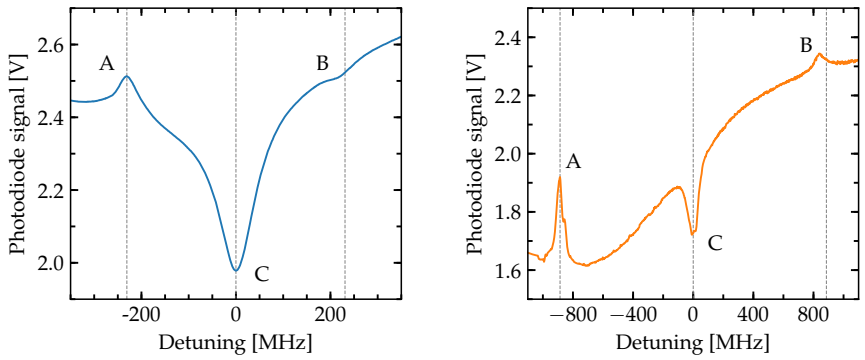

(a) SAS signal of ^{39}K.

(b) SAS signal of ^{23}Na.

Figure 4.5: Doppler-free absorption spectra of the D_2-line of potassium and sodium. The different transitions are labelled: A for $F = 2 \rightarrow F'$, B for the transition $F = 1 \rightarrow F'$, and feature C represents the crossover resonance.

with a Λ-system, with two ground states $F = 1, 2$ and a shared excited state F′, we observe a dip in the photodiode signal (i.e. transmitted intensity).

Moreover, we would expect feature B in figure 4.5a to be a peak instead of a dip. However, the coincidence of this transition with the ground state crossover of ^{41}K leads to the observed dispersive shape.

4.3 ZEEMAN MODULATION LOCKING

Saturated absorption spectroscopy, which was introduced in the last section, allows us to precisely locate the different hyperfine transitions. In the end we would like to stabilize the laser to one of these transitions, by adjusting its frequency accordingly.

However, since the amplitude increases on both flanks of the dip, a feedback controller would not know in which direction to apply the correction. On the other hand, the derivative signal is asymmetric around the resonance, which gives the controller a sense of directionality. This derivative signal is also known as an error signal.

Underlying principles of Frequency Modulation Spectroscopy (FMS)

Experimentally, this error signal can be produced using a technique known as Frequency Modulation Spectroscopy (FMS). A very basic model, illustrating how this scheme works is shown in figure 4.6.

The frequency of the laser is being periodically modulated at a low frequency ($\sim$ 10 kHz) and a low amplitude (see figure 4.6a). Once the laser is tuned close to the atomic resonance, the modulation of the frequency (FM) translates to an amplitude modulation (AM). The modulation of the amplitude depends on the frequency of the laser, as it is strongest where the transmitted intensity changes the most. Directly on resonance, however, it approaches zero. If we plot the ratio of AM to FM as a function of the laser frequency, we get the graph in figure 4.6b, which is exactly the derivative or error signal of the atomic resonance spectrum.

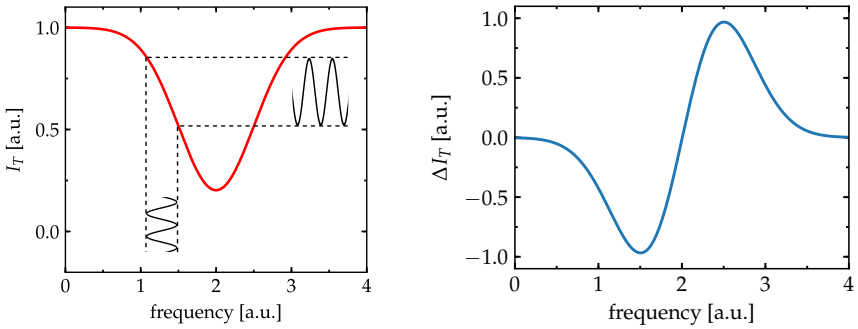

(a) Model absorption spectrum, with a frequency modulation on the left flank.

(b) Ratio of amplitude modulation to frequency modulation as a function of frequency.

Figure 4.6: Model for frequency modulation spectroscopy, where the modulation of the laser frequency translates to an amplitude modulation, resulting in an error signal.

To implement the FMS-approach, we could modulate the frequency of the laser by periodically changing the current, supplied to the laser diode, leading to the creation of sidebands.

Magnetic field modulation

Instead of directly changing the frequency of the laser, one can also modulate the absorption resonance frequency, by subjecting the atoms in the spectroscopy cell to a sinusoidally varying magnetic field [33, 34]. This has the same effect as FMS, but is much cleaner, since the laser, which we also use to generate the cooling light, is not affected.

In the experiment we achieve the magnetic field modulation by winding a copper wire around the vapour cell (see figure 4.3) and applying an alternating current to ends of the wire. We drive the coil, which has approximately 150 windings of Ø0.5 mm copper wire, with the amplified analogue output of a *Red Pitaya*.

LASER LOCK EMPLOYING A RED PITAYA The main features of the ADC system *Red Pitaya* are its two RF inputs and two RF outputs with 14 bit resolution and its Ethernet interface, with which this device can be accessed remotely. The amplification is performed by a commercial OPA548 power operational amplifier module.

Besides modulating the magnetic field, the *Red Pitaya* also functions as a lock-in amplifier, an oscilloscope and a digital PI-controller. All of these applications can be combined and controlled with the open-source graphical user interface *PyRPL*, which is accomplished in the following way:

1. We modulate the magnetic field by using the analogue output 1 from the *Red Pitaya* and the amplifier module. The frequency, phase and amplitude of the modulation are freely adjustable.

2. The modulated absorption spectrum, recorded by the photodiode, is fed into the analog input 1. This signal is then internally demodulated, resulting in an error signal.

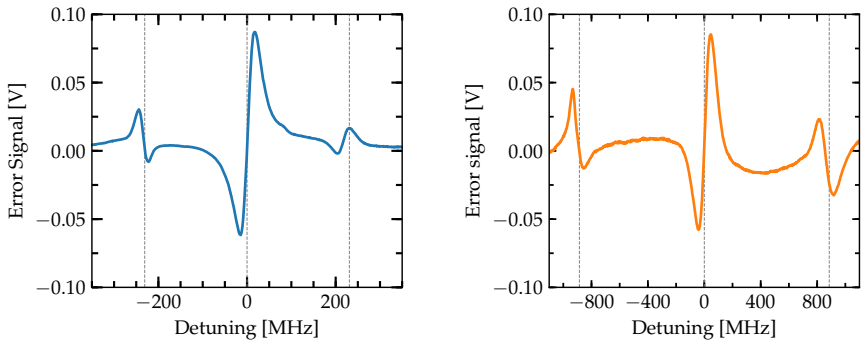

(a) Error signal of ^{39}K.

(b) Error signal of ^{23}Na.

Figure 4.7: Zeeman modulation of potassium and sodium. The magnetic field was modulated at a frequency of 15 kHz. The phase and amplitude of the modulation have been adjusted to optimize the strength of the central ground-state crossover feature.

3. The second output is connected to a fast input of the laser controller. Via analogue remote control, the *Red Pitaya* can now regulate the piezo-voltage of the laser. By applying a ramp signal to this output, we can visualize the typical dispersive shape of the error signal.

4. Lastly, the ramp is turned off and the digital PI-controller, with its adjustable P- and I-values, is activated. The laser can then be locked to the closest zero-crossing.

The generated error signals for potassium and sodium are shown in figure 4.7. The potassium light is stabilized to the ground-state crossover transition of ^{39}K (central feature in figure 4.7a), whereas we lock the sodium light to the excited-state crossover transition $3^2S_{1/2}\ |F = 2\rangle \ \rightarrow \ 3^2P_{3/2}\ |F' = 2, 3\rangle$ (left feature in spectrum 4.7b). Therefore, we have to optimize phase, frequency and amplitude of the modulation with respect to the strength of the corresponding feature.

4.4 SUMMARY

We have integrated a feedback mechanism, which locks the laser to an atomic resonance, obtained via a Doppler-free spectroscopy method. An error signal, which is proportional to the deviation of the laser frequency from the atomic reference, is generated by modulating the magnetic field inside the vapour cell. The feedback cycle is completed by a digital PI-controller, that adjusts the frequency of the laser accordingly.

All of this is achieved by a single device (*Red Pitaya*), which modulates the magnetic field, creates the error signal through an internal lock-in amplifier, and adjusts the laser frequency through a PI-controller.

5 LASER SYSTEM

For each atomic species we have one 750 mm x 1200 mm x 110 mm breadboard (Thorlabs B75120B), where the diode lasers and all the optics for frequency stabilization, light amplification and frequency shifting are located.

The two optical tables are stacked on top of each other, because of space constraints in the lab.

A side view of the laser tables is depicted in figure 5.1. The upper breadboard is supported by four 80 mm x 80 mm x 750 mm aluminium profiles (*Item*).

Since the layouts of the two laser systems for sodium and potassium are very similar, I will introduce the scheme set up for potassium in section 5.1 and then highlight the key differences for sodium in section 5.2.

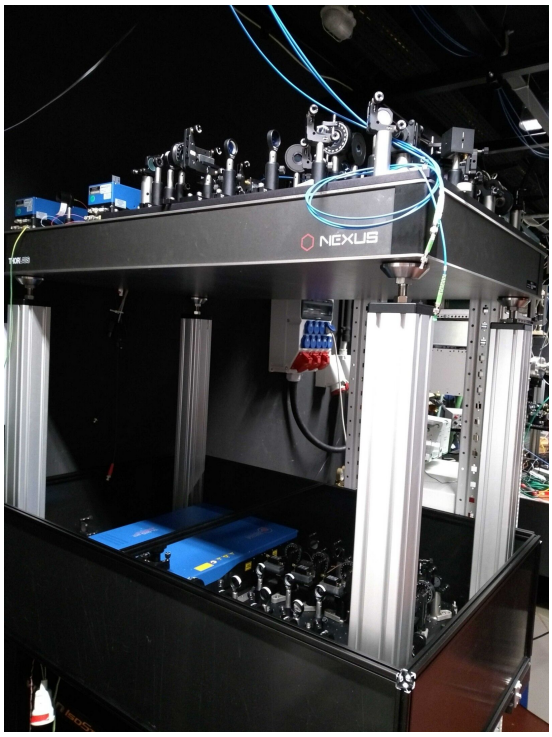

Figure 5.1: Side view of the two laser tables stacked on top of each other. The sodium optics are on the lower breadboard, while the potassium table sits on top.

5.1 POTASSIUM LASER TABLE

For potassium we have implemented the Master-Slave configuration. This means that we are using two tunable diode lasers, where the master laser is locked to an atomic reference as explained in chapter 4. The slave laser is stabilized to this reference via an Offset lock and provides all the cooling and repumping light for the experiment.

As illustrated in figure 5.2, the setup of the potassium laser table can be divided into four parts: the light from two diode lasers is frequency stabilized, amplified, split into multiple paths and finally shifted in frequency. In the following sections we will discuss these four steps in more detail.

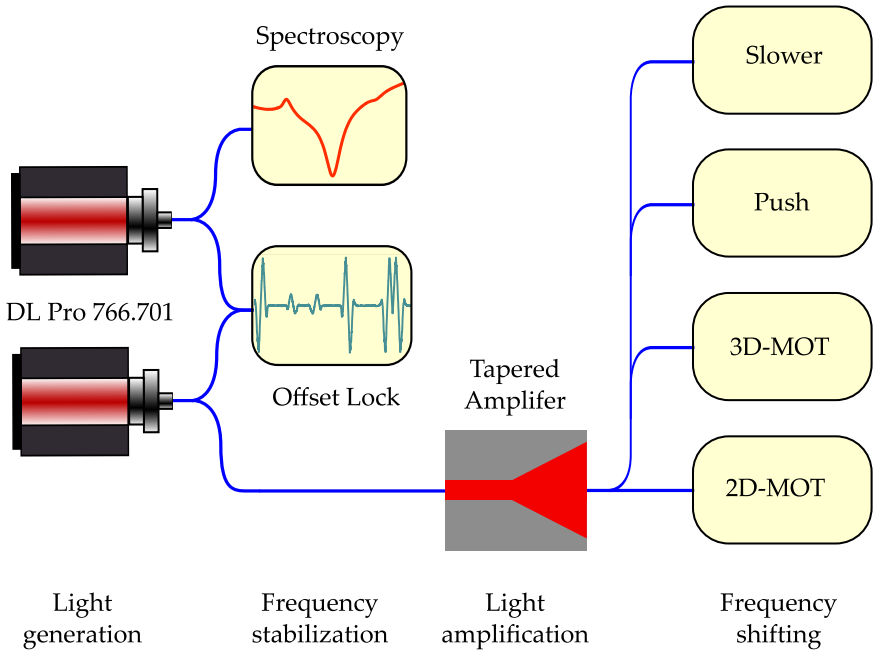

Figure 5.2: Overview of the optical layout on the potassium laser table, from which the different frequencies for cooling and trapping are produced.

5.1.1 *Light generation*

The potassium laser light is supplied from a tunable External Cavity Diode Laser (ECDL) in Littrow configuration (see figure 5.3). The divergent beam from the laser diode gets collimated and hits the diffraction grating.

In this configuration the first order gets reflected back towards the laser diode, whereas the 0th diffraction order forms the output beam. As the rear facet of the laser diode is anti-reflection coated, it forms an external cavity with the wavelength-selective grating. The optical feedback provided by the back-coupling of one specific frequency leads to a single-mode operation of the laser, which is determined by the geometry of the grating:

$$\lambda = 2\,d\,\sin(\theta) \tag{5.1}$$

where d: grating constant and θ: angle of incidence.

By turning the grating, i.e. changing θ, we are able to tune the output wavelength of the laser. The fine-adjustment of the emission frequency is experimentally achieved via a piezo-electric actuator that is attached

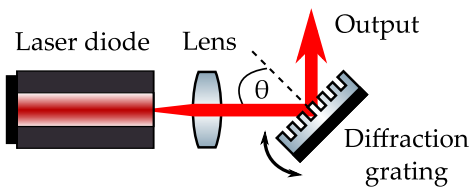

Figure 5.3: Schematic of an ECDL in Littrow configuration.

to the grating. The grating angle can be adjusted by supplying the actuator with the appropriate voltage (i.e. piezo voltage).

Altogether the advantages of a very narrow linewidth and a good tunability outweigh the problems with mode-hopping.

In the experiment, two tunable ECDLs (Toptica DL Pro) produce light at a wavelength of 766.701 nm. In the fiber-coupled version it can supply approximately 30 mW of power at a linewidth of approximately 50 kHz.

5.1.2 *Frequency offset lock*

The master laser is locked to the D_2 ground-state crossover line of ^{39}K. The slave laser is stabilized to this reference via an offset lock, using the beat signal generated when overlapping the two lasers outputs. This technique enables us to lock to any frequency offset with respect to the master laser. Switching between the two species ^{39}K and ^{40}K can then simply be achieved by changing the overall offset.

Frequency offset locking scheme

Figure 5.4 depicts the basic scheme of an offset lock [35, 36]. In the first step, light from the master (frequency ω_1) and slave laser (ω_2) is superimposed on a fast photodiode (*Hamamatsu* G4176-03). The superposition produces the sum and difference frequencies: $\omega_1 + \omega_2$ and $\Delta\omega = \omega_2 - \omega_1$. However, only the difference or beat signal, which is typically of the order of a few hundred MHz to a few GHz, is detectable with the photodiode.

Next, this beat signal is mixed with a radio-frequency signal (ω_{VCO}) from a Voltage-Controlled Oscillator (VCO). A low-pass filter cuts off the high-frequency part, so that only the difference signal $\Delta\omega - \omega_{\text{VCO}}$ remains.

In the third step the signal is split and one part is fed into a long coaxial cable. This cable is referred to as a delay line, since it introduces a frequency-dependent phase delay between the two split signals:

$$\Phi = (\Delta\omega - \omega_{\text{VCO}})\tau = \omega_{\text{err}}\tau \tag{5.2}$$

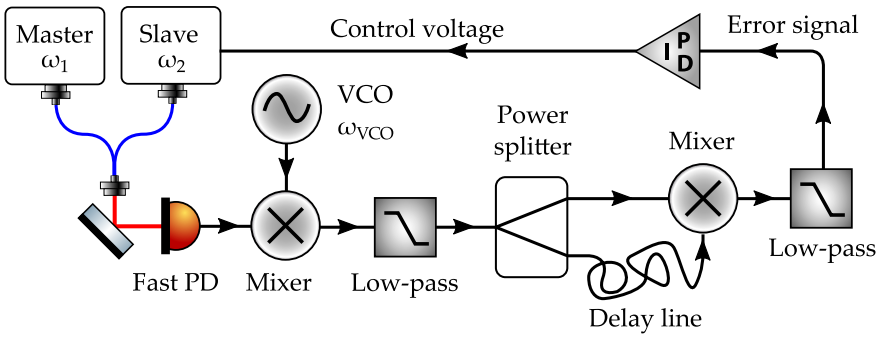

Figure 5.4: Frequency offset lock scheme using a delay line.

A 1 m long coaxial cable will lead to a time delay of $\tau \approx 5$ ns. Mixing the two signals with a second mixer results in:

$$\cos(\omega_{\text{err}} t)\cos(\omega_{\text{err}} t + \Phi) = \frac{1}{2}\left\{\cos(\Phi) + \cos(2\omega_{\text{err}} t + \Phi)\right\} \tag{5.3}$$

Removing the second part, that oscillates at $2\,\omega_{\text{err}}$, with another low-pass filter, finally results in the dc-signal $\cos(\Phi)$. This signal only depends on the frequency difference between the optical beat note and VCO-frequency, and the time delay given by the length of the coaxial cable.

Experimental implementation of the beat lock

In the experiment we adjust the VCO-frequency, which sets the desired offset. Next, we scan the slave laser's frequency ω_2 using the piezo-electric actuator. Following equation 5.3 and considering the phase Φ is linearly proportional to ω_2, one would expect a cosine-shaped error signal. However, the final low-pass filter distorts this profile. For a comprehensive description of the underlying electronic circuit please refer to [36].

The feedback loop is completed by feeding the error signal into a *Red Pitaya*, which functions as a digital PI-controller and adjusts the piezo-voltage or diode current of the slave laser via the external remote control.

The error signal, which is generated by our offset locking circuit, is displayed in figure 5.5. The master laser is locked to the spectroscopy and the slave laser scans the piezo voltage over a range of 800 MHz. In principle, we could now lock the slave laser to any slope. However, locking to the steepest slope with the largest peak-to-peak voltage increases the stability of the lock. In this case, it is the trailing edge, which crosses the origin (marked by the circle). For ^{39}K we are working at an offset of $\Delta\omega = -410$ MHz, whereas the offset for ^{40}K is set to $\Delta\omega = +406$ MHz.

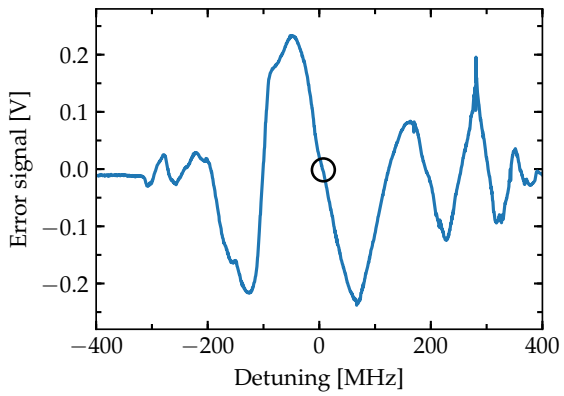

Figure 5.5: Error signal of the potassium offset lock. Several lock points indicated by the zero crossings are visible. For ^{39}K we locked to falling slope indicated by the circle.

5.1.3 *Light amplification*

At this stage, we have 30 mW of laser power that is stabilized to a variable frequency offset. In the following, we want to split up the light and use it for laser cooling, which requires higher laser power. Therefore the light from the slave laser is amplified by a home-built fiber-coupled Tapered Amplifier (TA) module.

Theory of a tapered amplifier

A TA chip, as shown in figure 5.6a, consists of two sections: a 3 μm thin straight waveguide followed by a tapered gain region with an output aperture of 190 μm. When a low power seed beam enters, the narrow waveguide filters out a single mode and leads to large energy densities [37].

In the tapered section, the light is amplified. The amplification is provided by an external current that is supplied to the gain medium. Due to the tapered shape of the medium, higher output powers are possible, since the energy density is reduced.

The gain medium, however, does not only amplify the seed beam, but also the spontaneous emission, occurring because of the large population inversion. While the Amplified Spontaneous Emission (ASE) is supressed at a high amplification current due to gain competition, it is particularly useful at low currents as a first alignment tool, since it does not require the in-coupling of the seed beam.

Optical setup

The setup of our TA module, which was designed by Florian Nicolai during his master's thesis [37], is depicted in figure 5.7. The tapered amplifier chip (*Eagleyard Photonics* EYP-TPA-0765-02000), which is mounted in a copper block (see figure 5.6b), is seeded from the output of the fiberized slave laser. Two folding mirrors couple the light into the TA diode. At the input and output facet, two aspheric lenses with a focal length of $f = 4.51$ mm focus the beam onto the centre of the chip. As the alignment of these lenses is very crucial, they are mounted on an XYZ-translation stage that is fixed to the copper block, which houses the chip, through a 30 mm cage system.

Owing to the geometry of the chip, the output is highly divergent, which is compensated for by a $f = 40$ mm cylindrical lens. Further

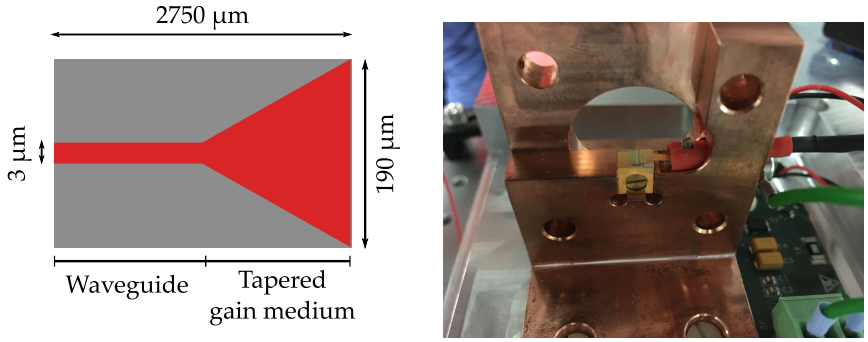

(a) Sketch of a TA chip.

(b) TA chip mounted in a copper block.

Figure 5.6: Sketch and image of a tapered amplifier diode.

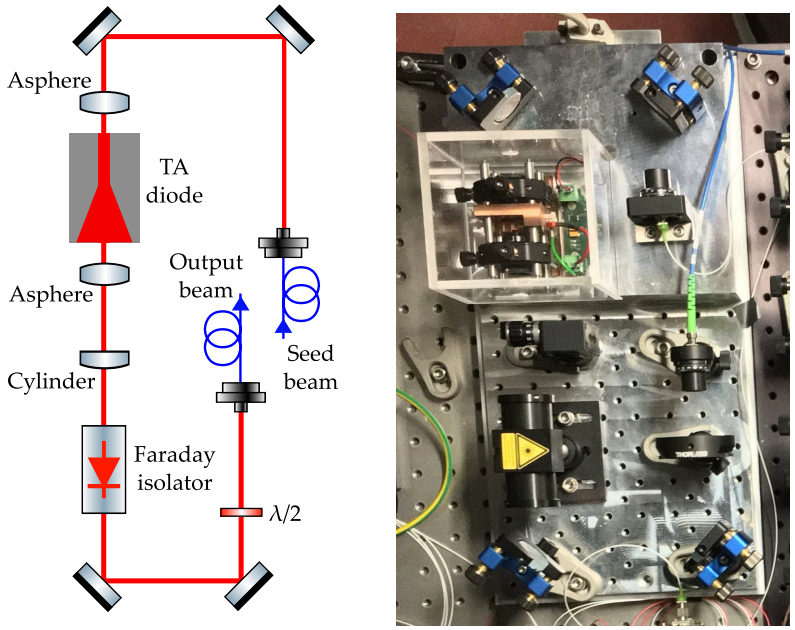

(a) Schematic of the TA optical setup.

(b) Image of the custom TA module after assembly and alignment.

Figure 5.7: Setup of the home-built fiberized TA module.

along the beam path, back-reflections that could damage the fragile TA-chip are eliminated by a Faraday isolator. With another two folding mirrors we eventually couple the amplified light into an optical fiber. The polarization maintaining coupling is accomplished, utilizing a half-wave plate in front of the fiber coupler.

The whole system is mounted on a 10 kg, 205 mm x 405 mm aluminium baseplate (see figure 5.7b). This plate not only improves stability, but also acts as a heat sink for the TA-chip. Consequently, no active cooling is required.

Protection circuit

As tapered amplifier chips are very sensitive devices, which can get permanently damaged by voltage spikes, there is a protection circuit bridging the gap between the current controller and the chip's cathode. Details on this circuit, such as a list of electrical components and their functions, are presented in [37].

Alignment procedure

After the mounting the necessary optics and optomechanics, detailed in the previous paragraph, we have to align the laser with respect to the amplifying chip. The alignment was performed following a comprehensive description in [34]. It entailed adjusting the XYZ-translation stages of the aspheric lenses by using the ASE. After aligning the seed side and obtaining an amplified output, the Faraday isolator and cylindrical lens are placed into the beam path. Finally, the light is coupled into an optical fiber. The initial alignment should be carried out at lower power, corresponding to a TA-current of 1 A. After increasing the current to its working value of 2.9 A, the coupling procedure has to be re-iterated.

Characterization of the TA-diode

To characterize the performance of our TA-chip, we performed a series of measurements. The results are depicted in figure 5.8. The output power was measured directly after the Faraday isolator, whereas the coupling power refers to the power recorded after the fiber coupler.

First of all, we measured the output power as a function of diode current for two different seed power values of $P_{\text{seed}} = 10$ mW and $P_{\text{seed}} = 20$ mW (see figure 5.8a). For both input power ratings, the output power showed a linear increase above a current of 1.25 A. Considering the Faraday isolators transmission efficiency of $\sim 80\%$ a measured value of ~ 1.6 W is in good agreement with the 2 W of power the TA-chip is specified for.

Next, we checked the input power dependence of the output power at a fixed current of 2 A, which is plotted in graph 5.8b. The output power first increases and then saturates above a seed power of ~ 17 mW. To achieve maximum amplification, we kept the seed power at ~ 20 mW during normal operation.

Moreover, we optimized the amplified power by examining its seed polarization dependence (figure 5.8c). Using a half-wave plate in front of the TA-chip, we rotated the input polarization by a total of 120 °. The power changes from its maximum value to almost zero, by rotating the seed polarization through 90 °. Consequently, we have to ensure the correct polarization of the seed beam.

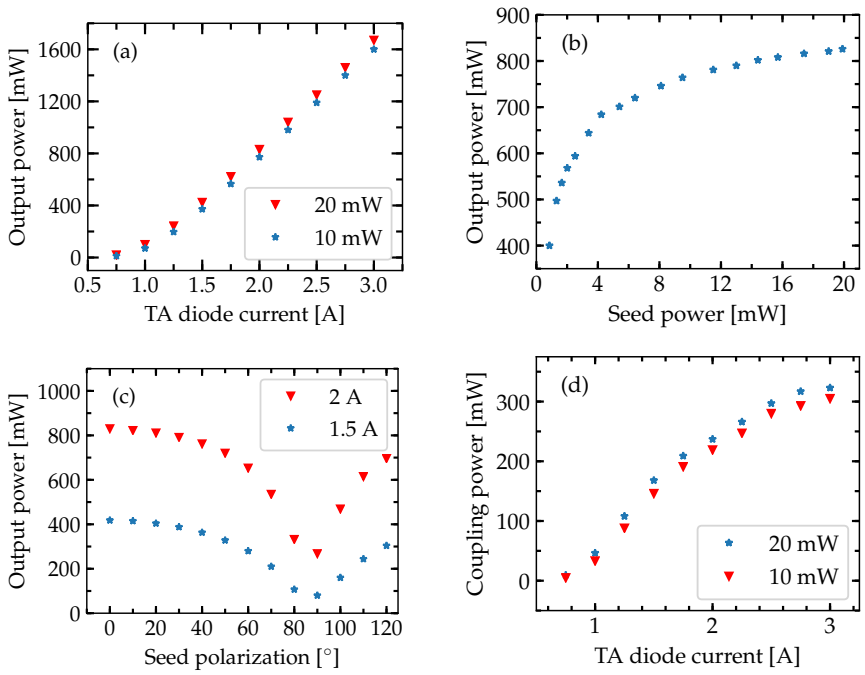

Figure 5.8: Characterization of the custom tapered amplifier module. (a) TA output power as a function of diode current for two different seed power values: 10 mW and 20 mW. (b) The output power saturates for increasing seed powers. (c) The output power also depends on the polarization of the seed beam, as it is shown for two different TA currents of 2 A and 1.5 A. (d) The coupling power increases as a function of diode current for both seed power ratings of 10 mW and 20 mW, but saturates at higher currents.

After exiting the Faraday isolator, the light is coupled into a single-mode fiber. Therefore, we also measured the coupling power at the exit of the fiber coupler as a function of the TA diode current, which is displayed in figure 5.8d. At lower currents the coupling power, similarly to the output power, increases linearly. However, the power saturates when increasing the diode current, which is partially due to the spatial mode profile becoming multi-mode. With the particular TA chip characterized here, we only achieved a coupling efficiency of approximately 20%, as a result of a poor performance of the chip.

5.1.4 *Frequency Shifting*

In the fourth and final step, we split the light coming from the tapered amplifier into multiple paths and shift their frequencies. As stated in chapter 2, we require a configuration of multiple counter-propagating laser beams, that are red-detuned with respect to a certain atomic transition, in order to cool and trap atoms. Therefore, we refer to these red-detuned beams as cooling beams.

Need for repumping beams

All the cooling beams in the experiment are superimposed with so-called repumping beams, which are tuned to a different transition. Let's take a look at the energy level diagram of ^{39}K in figure 4.2. Because the excited states are close in energy, a non-resonant excitation may excite atoms $F = 2 \rightarrow F' = 2$, from which they can relax to the $F = 1$ ground state. Here they are not affected by the cooling beam any longer, so that all the atoms would end up being stuck in this state. Consequently, this state is called a dark state.

In order to get these atoms out of the dark state, a so-called repumping laser beam, that is tuned to the transition $F = 1 \rightarrow F' = 2$, is used. This beam depopulates the $F = 1$ ground state and pumps the atoms back into the cycling cooling transition.

Design and operation of an AOM and EOM

We need to be able to change the frequency of the laser in a very controlled and efficient manner. The two most popular optical devices, with which we can shift the frequency of a laser beam, are:

ACOUSTO-OPTICAL MODULATOR: Consists of a crystal, which is attached to a piezo-electric transducer (see figure 5.9a). Standing sound waves, which are produced by applying an RF-input (ω_{RF}) to the transducer, are produced inside the Acousto-Optical Modulator (AOM) crystal. These standing waves (wave-vector $\mathbf{K}$) can also be thought of as density variations, which lead to a change of the refractive index. Therefore, the crystal acts as a diffraction grating, splitting the beam spatially ($\mathbf{k} + \mathbf{K}$) into multiple diffraction orders with a frequency spacing of ω_{RF} [38].

ELECTRO-OPTICAL MODULATOR: Makes use of the Pockels effect, which states that an electro-optic crystal's refractive index is proportional to an applied electric field. Consequently, a periodic modulation (frequency Ω) of the voltage supplied to the electrodes leads to a periodic change of the phase. This phase

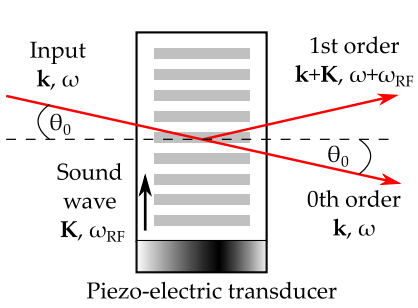

(a) Working principle of an AOM.

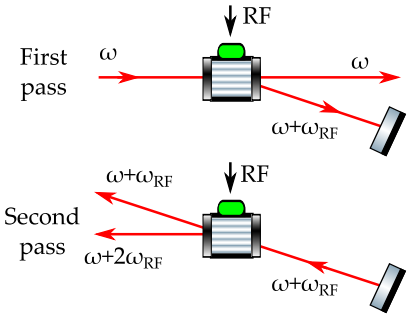

(b) AOM double-pass configuration.

Figure 5.9: Theoretical principle and experimental usage of an acousto-optical modulator (adapted from [38]).

modulation results in the creation of side-bands occurring at $\omega_c \pm \Omega$, with ω_c: carrier frequency. The frequency shift originates from transferring power into the sidebands while maintaining the beam direction.

For an AOM the diffraction efficiency (i.e. the amount of power in a higher order relative to the zero order) depends on the angle of the AOM crystal with respect to the incoming light, the size of the laser beam inside the crystal and the rf-input power. Hence, reaching a diffraction efficiency of 90% for the first order can only be achieved by careful alignment.

Furthermore, the diffraction angle depends on the modulation frequency. Therefore, changes or fluctuations in the frequency affect the beam direction. A stable alignment, however, is of great importance, because the light is coupled into single-mode fibres, which are very sensitive to these changes.

AOM double-pass configuration

To avoid this problem, the laser light is sent through the AOM twice, using the double-pass configuration [39], which is illustrated in figure 5.9b. In the first pass the 1st order emerges from the output facet of the modulator at a certain deflection angle and shifted in frequency by ω_{RF} with respect to the 0th order. By reflecting the scattered beam back through the AOM, the initial deflection is exactly cancelled out when looking at the 1st diffraction order of the second pass. As a result, we end up with a total frequency shift of $2\omega_{RF}$ and an output that is exactly superimposed with the input. As we are extracting twice the first order, this configuration is labelled (1,1). We separate in- and output through their polarization by placing a quarter-wave plate between the AOM and the retro-reflecting mirror. A PBS, eventually, separates the frequency-shifted output from the input.

On the optical table the beam first passes through a Galilean telescope, which reduces the beam diameter to match the aperture of the AOM.

Cat's eye retro-reflector

For the retro-reflector we use a cat's eye over a simple flat mirror, because it enhances the frequency tunability [39]. With a flat mirror

you can optimize the diffraction efficiency for one specific deflection angle corresponding to one distinct rf-frequency. Therefore, changing the rf-frequency leads to an imperfect alignment. However, a convex lens causes the diffraction orders to be parallel to each other, eliminating the deflection angle. As the multiple orders all hit the mirror at normal incidence, the alignment does not depend on the rf-frequency anymore. In our setup the cat's eye retro-reflectors consist of a 75 mm convex lens and a dielectric mirror.

Description of the potassium laser table

Now that we know how to shift the frequency of a laser by tens of MHz to a few GHz, we can have a look at the layout on the potassium optical table, that is shown in figure 5.10. This setup enables the creation of cooling and repumping light for both ^{39}K and ^{40}K.

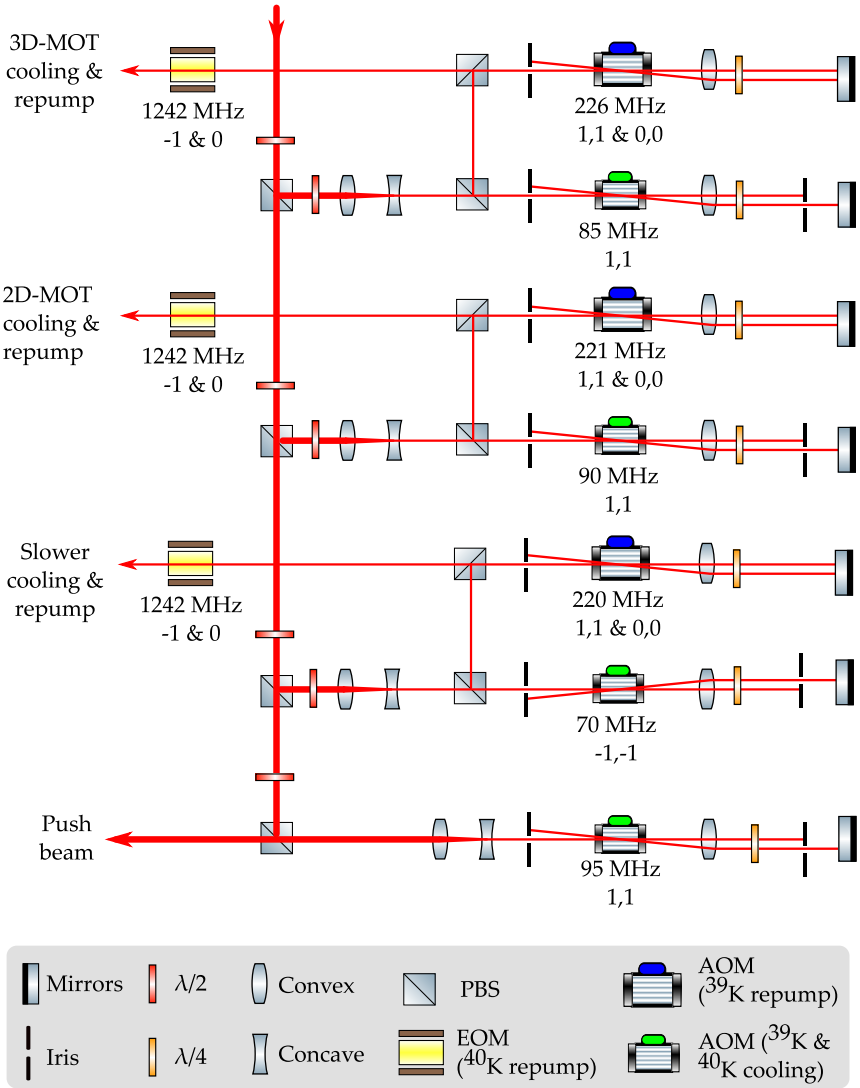

Figure 5.10: Schematic drawing of the optical layout on the potassium laser table for splitting and frequency shifting the amplified laser light. The numbers below the AOMs and EOMs represent the rf-frequency and the diffraction orders.

The respective cooling and repumping transitions are displayed in figure 5.11. The detuning with respect to these transitions is denoted by δ_{cool} and δ_{rep}.

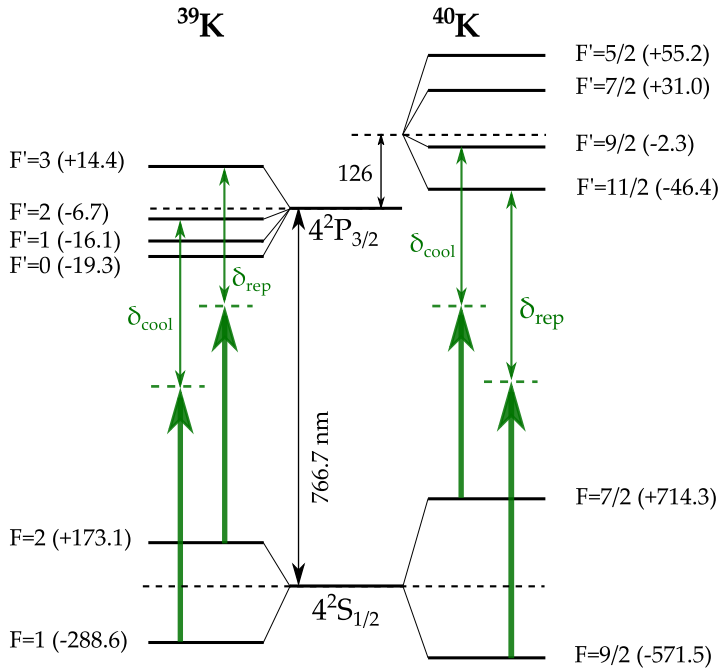

Figure 5.11: Cooling and repumping transitions of ^{39}K and ^{40}K (figure not to scale).

On the laser table we start out with the amplified fiber-coupled output of the tapered amplifier. The light is split into four paths: 3D MOT, 2D MOT, Zeeman slower and push beam. The first three paths are almost identical in their layout, whereas the push-beam path comprises a simple AOM double-pass as explained previously. The relative intensities of the different paths can be adjusted by a combination of a half-wave plate and a PBS.

In the 3D MOT path, the beam diameter is firstly reduced by a Galilean telescope. We are using an $f = -50$ mm plano-concave and $f = 150$ mm plano-convex lens (f: focal length), resulting in a demagnification of 3:1. The beam then passes through the first AOM, which is tuned to $\omega_{\text{RF}} = 85$ MHz, twice. Blocking the 0th order both times, we end up with the (1,1)-order and a total shift of $\omega_{\text{shift}} = +170$ MHz. At this stage we already have the ^{39}K cooling light for the 3D-MOT.

Through a polarizing beam splitter, positioned between the telescope and the AOM, the beam is coupled into a second double-pass. The optical modulator at $\omega_{\text{RF}} = 226$ MHz is responsible for the creation of the ^{39}K repumping light. The alignment of this AOM turned out to be particularly challenging as the (0,0) and the (1,1) orders have to be perfectly overlapped, when being coupled into a single-mode fiber. Furthermore, we loose 50% of the light, since we are blocking the (0,1) and (1,0) orders. We end up with a total shift of $\omega_{\text{shift}} = +170$ MHz for the (0,0) beam and $\omega_{\text{shift}} = +622$ MHz for the (1,1) beam.

The 2D MOT and slower paths work accordingly with slightly different AOM frequencies.

In case we want to switch from ^{39}K to ^{40}K, the offset is changed via the beat lock, the second AOM is turned off and the EOM is actuated. The overall offset in combination with the first double-pass creates the ^{40}K cooling light. The EOM, at a frequency of $\Omega = 1242$ MHz, generates the repumping light with its -1st order.

To transport the light from the laser table to the main experimental table, where the vacuum system is installed, we are using single-mode optical fibers. The core of such a fiber is surrounded by a cladding material with a lower refractive index. By means of total internal reflections off the cladding, light is guided through these wave-guides with low internal losses. Moreover, these fibers maintain the input polarization.

Table 5.1 summarizes the frequency detunings and intensities of the various ^{39}K and ^{40}K beams resulting from the setup shown in figure 5.10. A visual representation of the energy levels and the different frequencies can be found in Appendix B. There are no reported intensity values listed for ^{40}K, as we have not fully set it up yet. Once a 2D- and 3D-MOT of ^{39}K have been achieved, we will add the EOMs and switch to ^{40}K.

The detunings come about when locking the master laser to the ground-state crossover transition of the D_2-line of ^{39}K ($\delta_{\text{cool}} = +214$ MHz), then adding an offset of -410 MHz and finally shifting the frequencies with the help of AOMs and EOMs.

For the MOTs we chose a red-detuning of a few linewidths ($\Gamma/2\pi \approx 6.04$ MHz). The Zeeman slower, on the other hand, needs a large detuning, which is determined by the velocity of the effusing atoms and the magnetic field gradient along the slower axis. The optimal detuning values, however, will be determined when characterizing the magneto-optical traps.

Table 5.1: Overview of the values for detuning and intensity (per beam) of ^{39}K (left) and ^{40}K (right) laser beams. The saturation intensity is $I_S = 1.75$ mW/cm^2. δ_{cool} and δ_{rep} refer to the detunings shown in figure 5.11.

	δ_{cool} [MHz]	δ_{rep} [MHz]	Intensity [mW/cm^2]	δ_{cool} [MHz]	δ_{rep} [MHz]
2D MOT	-16	–	5.73	-10	–
3D MOT	-26	–	1.91	-20	–
Slower	-335	–	–	-330	–
Push beam	-5	–	14.15	0	–
2D MOT rep	–	-15	4.46	–	-10
3D MOT rep	–	-15	1.91	–	-20
Slower rep	–	-335	–	–	-330

Power-wise we are currently limited by the bad performance of the TA chip, the setup of our second AOM, with which we can only achieve a maximum efficiency of 50%, as well as a poor fiber coupling. Nevertheless, the intensities in the 2D- and 3D-MOT are above the saturation intensity, fulfilling the requirement for the MOT to function.

5.2 SODIUM LASER TABLE

Laser cooling and trapping of sodium atoms is achieved via the D_2-line located at a wavelength of $\sim$ 589 nm. However, there are no laser diodes in this operating regime available. The TA-SHG Pro laser (*TOPTICA Photonics*) circumvents this issue by frequency-doubling the output of a laser diode at $\lambda = 1178$ nm. A schematic of the laser is attached in figure 5.12.

Sodium light generation

The output of an external cavity diode laser in Littrow-configuration outputs light at a wavelength λ. A Faraday isolator makes sure that there are no back-reflections, which would damage the laser diode. The beam is then directed into a tapered amplifier by two folding mirrors. The TA amplifies the 20 mW input from the DL Pro to approximately 2 W.

Up until this point, we are dealing with the same setup as in the case of potassium. The only difference is that, here, we are working in the infra-red regime.

The amplified light is then guided into a resonant doubling cavity by two more folding mirrors. A telescope and a focusing lens

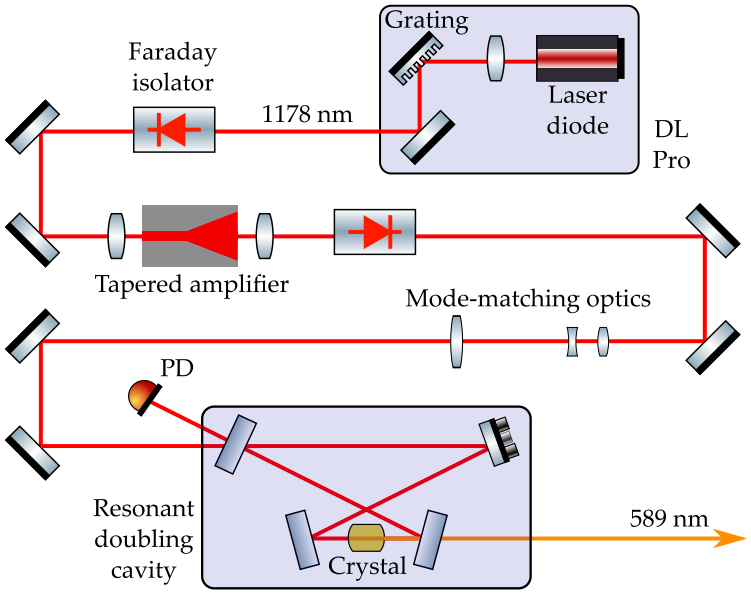

Figure 5.12: Schematic of the TA-SHG Pro (*TOPTICA Photonics*), which serves as our sodium laser. The output of an external cavity diode laser in Littrow-configuration gets amplified by a TA module and then frequency-doubled in a resonant doubling cavity, which results in a 1.6 W output at 589 nm.

shape the beam beforehand, in order to optimize the laser-to-cavity mode-matching. In this ring cavity in bow-tie configuration the beam passes through a non-linear crystal. The non-linear effect known as Second-Harmonic Generation (SHG) leads to a doubling of the laser frequency. Finally, roughly 1.6 W of 589 nm laser light exits the laser system through a shutter.

Frequency shifting optics

Compared to the potassium table, the frequency generation setup for sodium, shown in figure 5.13, is much simpler. It includes four AOM double passes and one single pass, as well as three EOMs generating the repumping light.

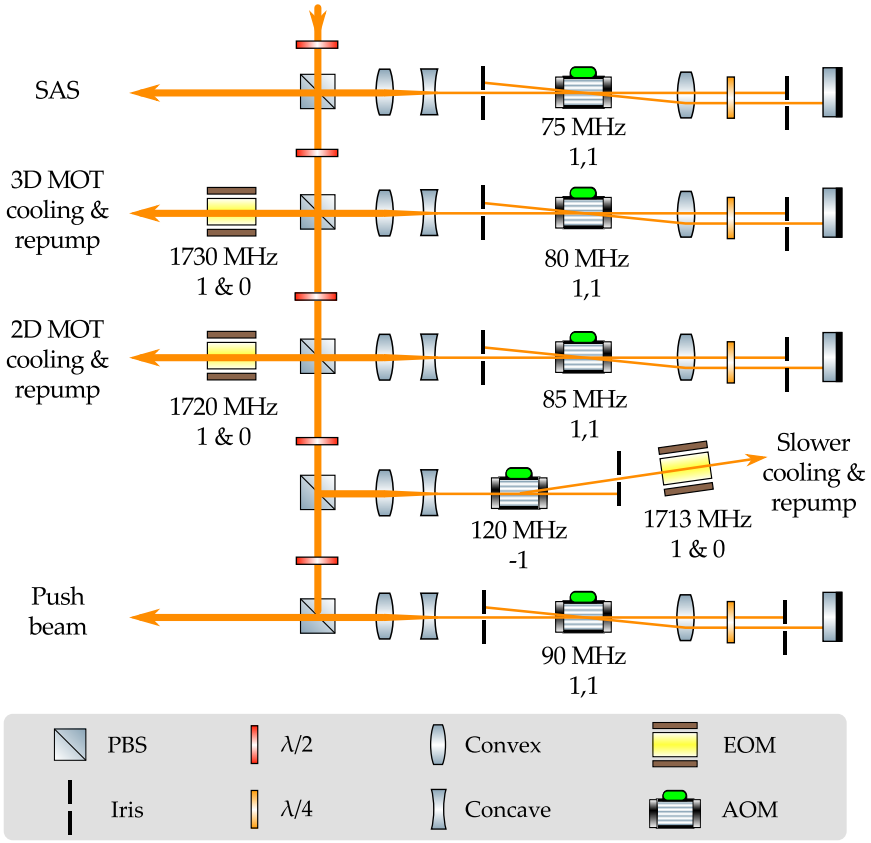

Figure 5.13: Optical layout on the sodium laser table. The light from all paths, except the spectroscopy path, is coupled into single-mode fibers.

However, unlike in the case of potassium, one double pass is dedicated to the spectroscopy. By shifting the light by 150 MHz and then sending it into the SAS setup, we effectively lock the laser at an offset with respect to the locking transition ($F = 2 \rightarrow F' = 2, 3$). Therefore, the light from the sodium laser is 179 MHz red-detuned wrt. to the cooling transition ($F = 2 \rightarrow F' = 3$) of ^{23}Na. For potassium, on the other hand, we utilized a beat lock to achieve a more flexible frequency offset.

As the sodium laser table is still a work in progress, table 5.2 includes projections on the detunings and intensities of the different laser beam paths. We are looking to work with cooling light, which is

Table 5.2: Overview of the projected values for detuning and power in various ^{23}Na laser beams. The saturation intensity is 6.26 mW/cm^2. The corresponding energy level diagram is attached in Appendix B.

	TRANSITION	DETUNING* [MHz]	POWER [mW]
2D MOT	$F = 2 \rightarrow F' = 3$	-9	116
3D MOT	$F = 2 \rightarrow F' = 3$	-19	250
Slower	$F = 2 \rightarrow F' = 3$	-299	73
Push beam	$F = 2 \rightarrow F' = 3$	$+1$	5
2D MOT rep	$F = 1 \rightarrow F' = 2$	-2	92
3D MOT rep	$F = 1 \rightarrow F' = 2$	-2	35
Slower rep	$F = 1 \rightarrow F' = 2$	-299	4

*The detuning is given wrt. the transition in the second column.

slightly red detuned with respect to the cooling transition $|F = 2\rangle \rightarrow |F' = 3\rangle$ and repumping light that is close to resonance with the transition $|F = 1\rangle \rightarrow |F' = 2\rangle$.

5.3 SUMMARY

In this chapter we have described the two independent laser systems, which allow us to produce the necessary light for laser cooling of sodium and potassium (^{39}K and ^{40}K). The output of a laser diode in Littrow-configuration is locked to an atomic transition, amplified, divided into multiple paths, shifted in frequency and eventually coupled into optical fibers. These fibers transport the light from the two laser tables over to the science table, where the vacuum apparatus is located.

6

IMPLEMENTATION OF THE 2D MAGNETO-OPTICAL TRAPS

The two two-dimensional magneto optical traps represent the first stage of cooling and serve as a source of cold atoms. Along with the cooling, provided by four counter-propagating laser beams, magnetic fields introduce a spatially-dependent force that confines the atomic clouds in two dimensions.

In the first part of this chapter, the necessary optics to produce the cooling beams is discussed. The second section focuses on the special magnetic field configuration consisting of permanent magnets. After describing the use of these magnets, I will present their features in terms of numerical simulations. The last section is devoted to fluorescence measurements within the 2D-MOT.

6.1 OPTICS

The light from the potassium and sodium laser tables is coupled into 10 m long optical single-mode fibers and transferred to the science table. Here, the light is multiplexed and expanded.

The optical layout of the 2D MOT is depicted in figure 6.1. Since we are trapping two species in two different chambers, there is one setup for potassium and one for sodium. The only difference between them being the coating of the lenses and the wave plates.

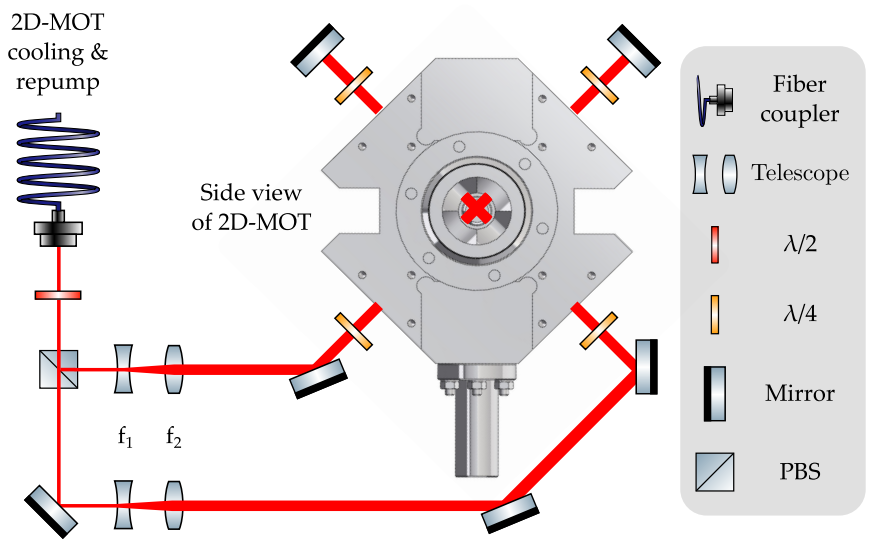

Figure 6.1: Schematic of the optical layout for the 2D MOT. The light is split, expanded, guided through the chamber and retro-reflected on the opposite side.

First of all, the light is split into two beams with equal intensities by using a half-wave plate and a PBS. Then, the beams are expanded employing a telescope with $f_1 = -2.5$ mm and $f_2 = 10$ mm, resulting in a final beam diameter of ~ 10 mm. For a MOT to function, the light needs to be circularly polarized, which is accomplished through the use of two quarter-wave plates in front of the chamber viewports.

Because we are restricted in power for both species, the 2D-MOTs are operated in a retro-reflected configuration. A second quarter-wave plate makes sure that the light keeps its handedness despite being reflected off a mirror at normal incidence. All mirrors in the setup are silver mirrors, as dielectric mirrors alter the polarization of the beam.

6.2 MAGNETIC FIELDS

Inspired by the design of Lamporesi et al. [28] and Tiecke et al. [40], we employed neodymium bar magnets to generate the required magnetic quadrupole field inside the chamber.

Why permanent magnets?

When compared to regular magnetic field coils, where an electric current running through a copper wire produces a magnetic field, these bar magnets have some advantages (+) and disadvantages (–):

+ Permanent magnets are very easy to handle and install. No extra equipment, such as power supplies, is needed, thus lowering the cost.
+ The vacuum setup is very compact and does not allow for too much space for coils.
+ The magnets are also used in a Zeeman slower configuration, producing a magnetic field gradient along the slower direction.
+ Less fluctuations in the field increase the stability during operation of the 2D-MOT.
– We cannot switch the magnets off or vary their field strength so easily.

Considering that we do not necessarily need to tune the field strength at this stage of the cooling process, we utilized permanent magnets for the 2D-MOTs.

Characteristics of the magnets

We used neodymium bar magnets (*ECLIPSE* N750-RB), which have the dimensions 3 mm x 10 mm x 25 mm. The magnetic dipole moment of each magnet is oriented along the 3 mm thin x-axis. The magnetic field at a position $\mathbf{r}$ generated by a magnetic dipole $\mathbf{m} = \mathrm{m}\,\mathbf{e}_x$ at position $\mathbf{r}_0$ reads:

$$\mathbf{B}(\mathbf{r}) = \frac{\mu_0}{4\pi}\left\{\frac{3(\mathbf{r}-\mathbf{r}_0)\,[\mathbf{m}(\mathbf{r}-\mathbf{r}_0)]}{|\mathbf{r}-\mathbf{r}_0|^5} - \frac{\mathbf{m}}{|\mathbf{r}-\mathbf{r}_0|^3}\right\} \tag{6.1}$$

with the vacuum permeability μ_0.

As a first step, we measured the distance-dependence of the magnetic field created by a pair of two magnets, in order to determine

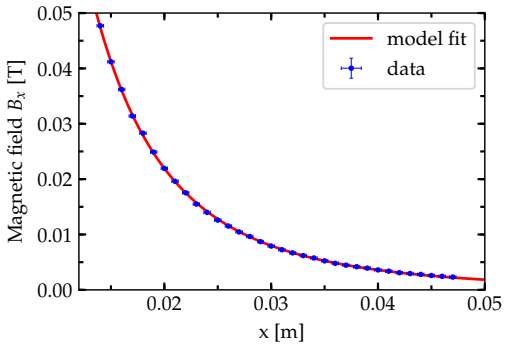

Figure 6.2: Measured magnetic field along the dipole moments direction for two magnets together with a model fit.

the magnetization of the permanent magnets. The field was measured along the x-direction using a Bell Series 5100 Gaussmeter on a linear translation stage with millimetre precision. The resulting data along with the theoretical model (using equation 6.1) is plotted in figure 6.2. The model fits well to the experimental data, resulting in a magnetization for a single magnet of:

$$M = 9.9(1) \times 10^5 \text{ Am}^{-1}$$
$$m = 0.74(1) \text{ Am}^2$$

The accuracy in the measurement was limited by the precision of the Gaussmeter and the accuracy of the translation stage.

Quadrupole configuration

With a maximum operating temperature of 80 °C, these magnets can produce a uniform quadrupole field when placed in the configuration shown in figure 6.3. In total, there are four stacks of multiple magnets located at $(x, y, z) = (0, \pm 37, \pm 49)$ mm, whereby the origin

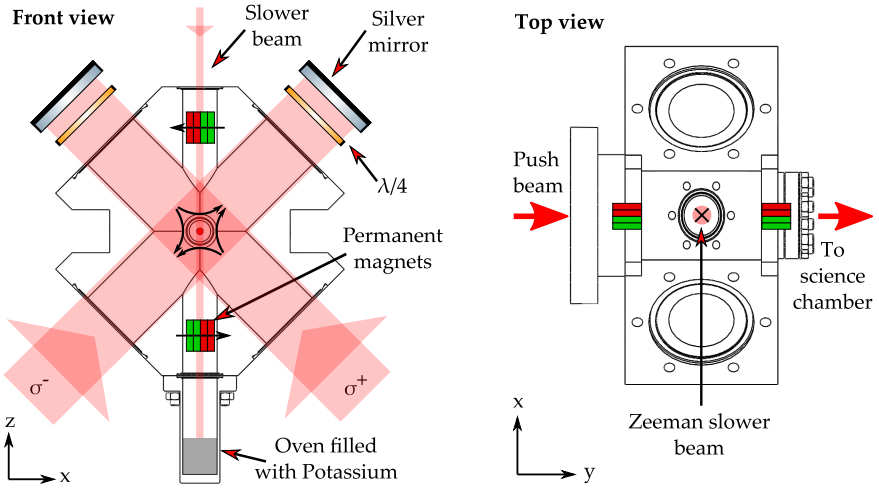

(a) Front view of the 2D-MOT chamber. The atoms are trapped in the center, marked by the red dot.

(b) Top view of the 2D-MOT chamber with the top two stacks of magnets in the same orientation.

Figure 6.3: Schematic of the 2D-MOT magnetic field. The stacks of permanent magnets are placed at $(x, y, z) = (0, \pm 37, \pm 49)$ mm.

is positioned at the centre of the chamber, where the atomic cloud is trapped. For potassium we are using two magnets per stack and there are nine magnets per stack for sodium. The directions of (x, y, z) are established through the coordinate system shown in figure 6.3.

To generate a quadrupole field in the xz-plane, the two stacks located at $z = \pm 49$ mm (fixed y) have to be orientated in opposite directions (see figure 6.3a). However, along the y-axis we do not want any trapping field, as the atoms are meant to be pushed in this direction through the differential pumping stage into the UHV-region. Consequently, the magnets at $y = \pm 37$ mm (fixed z) have the same orientation as seen in figure 6.3b. Locking down onto the chamber from above, the Zeeman slower beam goes along the z-axis into the xy-plane.

Fixing the orientation of the magnets also fixes the polarisation of the laser beams required to trap the atoms. The two incoming beams need to have opposite circular polarisation: σ^- and σ^+. As the magnetic field gradients are exactly inverted with respect to each other, both beams should have left-hand circular polarization.

Numerical simulation

To gauge the placement and strength of the magnets, we calculated the magnetic field numerically utilizing equation 6.1. Thereby we followed the considerations outlined by Donadello [30]. The total magnetic field, generated by the four stacks of magnets, can be extracted by summing up all contributions, leading to the results shown in figure 6.4. Here, we simulated the potassium 2D MOT, where we have two magnets per stack.

The total magnetic field in the xz-plane, which is depicted in figure 6.4a, possesses two maxima at the positions of the two magnet stacks ($z = \pm 49$ mm). Moreover, the magnetic field lines in the centre demonstrate the quadrupolar shape of the magnetic field. Setting $x = 0$ and plotting the dependence of the x-component of the magnetic field as a function of z-position, results in the graph shown in figure 6.4b. The Zeeman slower acts along this axis. The combination of a red-detuned laser beam with this spatially varying magnetic field leads to the

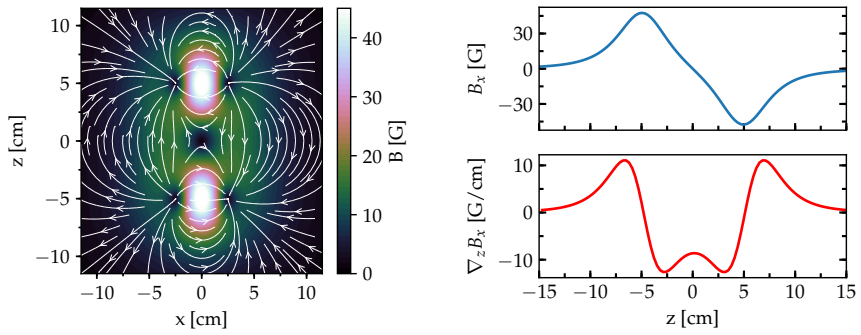

(a) Magnetic field in the xz-plane for $y = 0$. The magnetic field lines are indicated by white arrows.

(b) Numerical simulation of the magnetic field and its gradient along the Zeeman slower axis.

Figure 6.4: Numerical characterization of the K 2D-MOT magnetic field.

slowing and eventual capture of atoms effusing from the oven.

Experimental characterization of the magnetic field in the K 2D-MOT

Aside from the magnetic field gradient along the Zeeman slower direction, we are further interested in the gradient along the propagation direction of the four MOT beams. This gradient determines how many atoms (if any at all) can be captured. Therefore, we placed stacks of two magnets in the quadrupole configuration (as in the potassium 2D-MOT) on a 3D printed model of the 2D-MOT chamber. The magnetic field was measured along the diagonal cooling beam direction using the Gaussmeter on a linear translation stage.

The results of this measurement together with the numerical calculation and a linear fit are summarized in figure 6.5. The simulation correlates well with the experimental data. A linear regression provides us with the magnetic field gradient in the K 2D-MOT:

$$\nabla_{xz} B = 14.29(1)\ \mathrm{G/cm}$$

As the 2D-MOT of potassium has recently been accomplished with a similar configuration of permanent magnets but with a gradient of 30 G/cm [41], we will increase the number of magnets per stack to four, thereby doubling the gradient.

On the other hand, four stacks of nine magnets produce the quadrupole field for sodium, resulting in a magnetic field gradient along the cooling light propagation direction of ~ 65 G/cm.

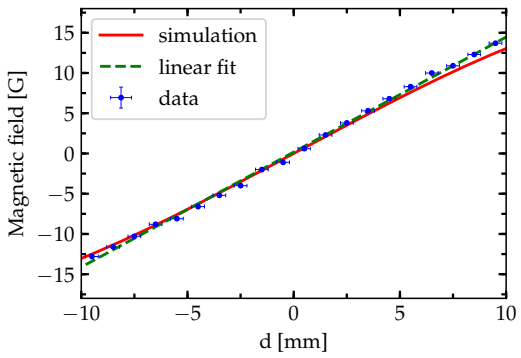

Figure 6.5: Magnetic field along the propagation direction of one of the cooling beams in the K 2D-MOT. Measurement data (blue points) with a linear fit (green dashed line) is compared to the numerical simulation, represented by the red curve.

6.3 FLUORESCENCE

After heating up the potassium oven to about 50 °C and sending the laser beams through the chamber, we were able to record the resulting fluorescence (see figure 6.6).

To acquire this picture, we placed a CMOS-camera (*MAKO* G-030) with an appropriate objective in front of the push-beam viewport. However, the push beam has to be placed directly in line of sight with the differential pumping tube. Otherwise, the atoms would not reach the science chamber, but would rather get pushed onto a wall.

Therefore, we had to install the camera at a tilted angle with respect the viewport.

Having the fluorescence signal, already provides us with information regarding certain experimental parameters. First of all, we can be sure that the laser beams are tuned to the correct frequency region. Fine adjustments can be performed by changing the corresponding AOM frequency and monitoring the intensity of the fluorescence. Furthermore, the fluorescence makes the beams, which propagate through the chamber, visible. This in turn can be used to align the beams so that they cross exactly in front of the differential pumping stage.

Eventually, we should be able to observe the 2D-MOT, identified by a bright spot in front of the differential pumping stage, via this imaging system. In previous attempts we could not make out a clear signal. However, by disturbing the magnetic field inside the chamber, we did notice some disturbances in the fluorescence signal.

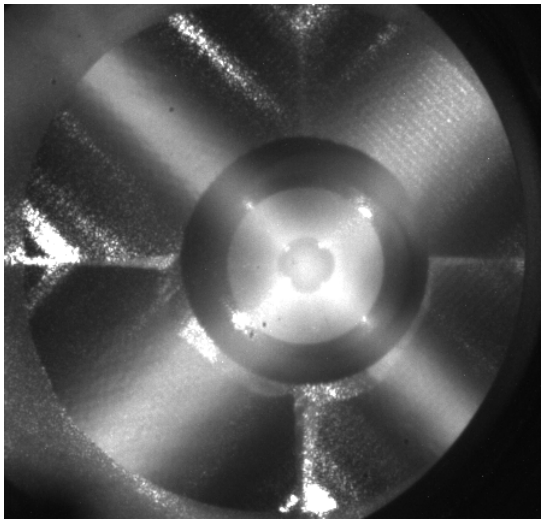

Figure 6.6: Fluorescence in the potassium 2D-MOT. The beams cross in the center in front of the differential pumping stage. The image has been taken at a tilted angle, because the push beam optics were blocking the direct view.

6.4 SUMMARY

In this chapter we discussed the setup of the 2D-MOT. The hot atoms effusing from the oven are slowed down by a Zeeman slower beam and are captured in a quadrupole field generated by neodymium bar magnets. The four counter-propagating, circularly polarized laser beams perform the first stage of cooling.

7 DUAL-SPECIES MAGNETO-OPTICAL TRAP

In the 2D-MOT the atoms are captured from the atomic vapour, that effuses from the oven. The near-resonant push beam transfers the atoms through the differential pumping stage into the UHV-section. In the science chamber the atoms are recaptured in a dual-species 3D-MOT.

This chapter gives an overview of the experimental implementation of the dual-species magneto-optical trap in terms of optics and magnetic fields. Additionally, some first experimental efforts to obtain a MOT of ^{39}K-atoms will be described.

7.1 OPTICS

In contrast to the 2D MOT, where each atomic species has one separate chamber, there is only one 3D MOT chamber (the science chamber), which is used for both sodium and potassium.

For each atomic species there is one breadboard for splitting the light into three beams, which are labelled as X, Y and Z (see figure 7.1a). The X-, Y- and Z-beams for the two species are overlapped using dichroic mirrors and then guided through the science chamber. Once the beams pass through the chamber, they are retro-reflected on the other side. The retro-reflector is mounted in a 30 mm cage system and consists of an achromatic quarter-wave plate, which covers a wavelength range of 400 – 800 nm, and a protected silver mirror. We

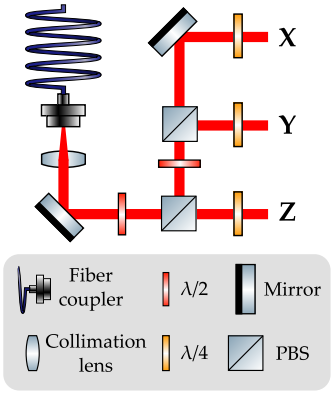

(a) Splitting optics breadboard. There is one for each atomic species.

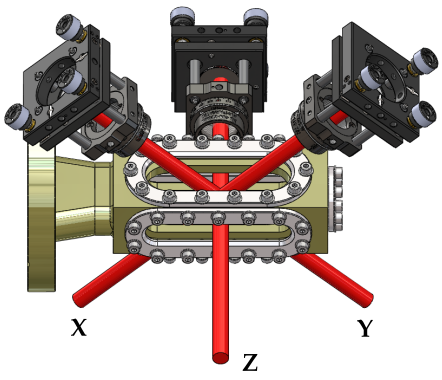

(b) 3D view of the MOT optics near the science chamber. The cage systems consist of an achromatic quarter-wave plate and a retro-reflecting silver mirror.

Figure 7.1: Schematic of the optical layout for the 3D MOT. The beam, containing the cooling and re-pumping light, is split into three beams (X, Y and Z), which are guided through the science chamber in a retro-reflected configuration.

need an achromatic wave-plate, as we are dealing with sodium light at 589 nm and potassium light at 767 nm.

A 3D-view of the chamber with the cooling beams and the retro-reflectors is shown in figure 7.1b. The Z-beam goes through the viewports on the sides (front and back), whereas the X- and Y-beams pass through the top and bottom viewport at $\pm 45^\circ$ angles.

Following the polarization convention, discussed in section 2.3, the X- and Y-beam have to have the same handedness. The Z-beam should be of opposite handedness. It depends on the magnetic field gradient, i.e. the direction of current running through the magnetic coils, if both X- and Y-beams are left-handed and the Z-beam is right-handed polarized or if it is the reverse configuration.

7.2 MAGNETIC COILS CONFIGURATION

The magnetic field coil configuration around the science chamber is displayed in figure 7.2. It consists of three different coil systems:

- MOT coils: produce the magnetic field gradient during the loading phase.
- Feshbach coils: generate large bias magnetic fields (several 100 G) to tune inter- and intra-species Feshbach resonances.
- Compensation coils: create small bias fields (few Gauss) to compensate undesired fields such as the earth's magnetic field.

The MOT coils are placed on the sides of the science cell, whereas the Feshbach coils will be fixed below and on top of the cell. Due to the

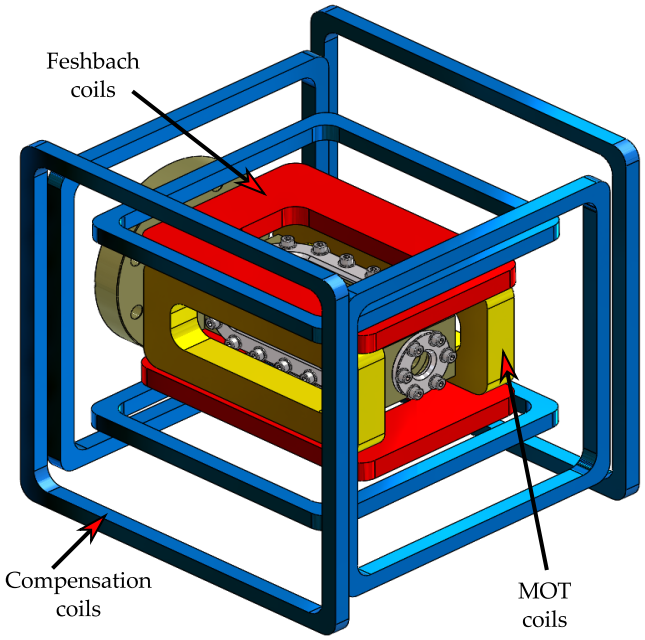

Figure 7.2: 3D schematic of the magnetic coils surrounding the science chamber. There are three types of coils: Feshbach coils (red), compensation coils (blue) and MOT-coils (yellow).

separation of MOT and bias coils, we are able to tune and switch these coils independently, which enhances modularity. However, as evident from figure 7.2, this choice constrains the limited space even further, which has to be considered when designing the coils and their holders.

In what follows, we will focus on the MOT coils, which have been designed, constructed and characterized in the course of this thesis and are shown in figure 7.3.

COIL HOLDER DESIGN For each coil, a copper wire is wound around four aluminium profiles, which are screwed together at all four corners. We selected aluminium because of its low cost, machinability and rigidity.

Circumventing the problems of hollow-core water-cooled coils, such as possible leakage, high water pressure and inefficient cooling, we designed the coils and their holders such that passive cooling is sufficient. This also limits the amount of current that can be sent through the coils, as the dissipated power is proportional to the square of the current. As a rule of thumb, coils with current densities up to 5 A/mm^2 do not require any active cooling [42]. To check the temperature of the coil during operation, we placed a thermocouple, which can be seen in the side view in figure 7.3, inside the coil between two windings.

Because of the elongated shape of the science cell, rectangular coils with one longer and one shorter axis (i.e. racetrack shape) are favourable (see figure 7.3). We incorporated u-shaped aluminium profiles with a length of 120 mm for the long sides and 30 mm for the short sides of the racetrack. The u-shape helps for guidance during the winding process, as it ensures that the coil does not fall out of the holder. The coil holders are mounted to the optical table via 1.5 inch posts, which are fixed to the holders via rectangular aluminium connection pieces.

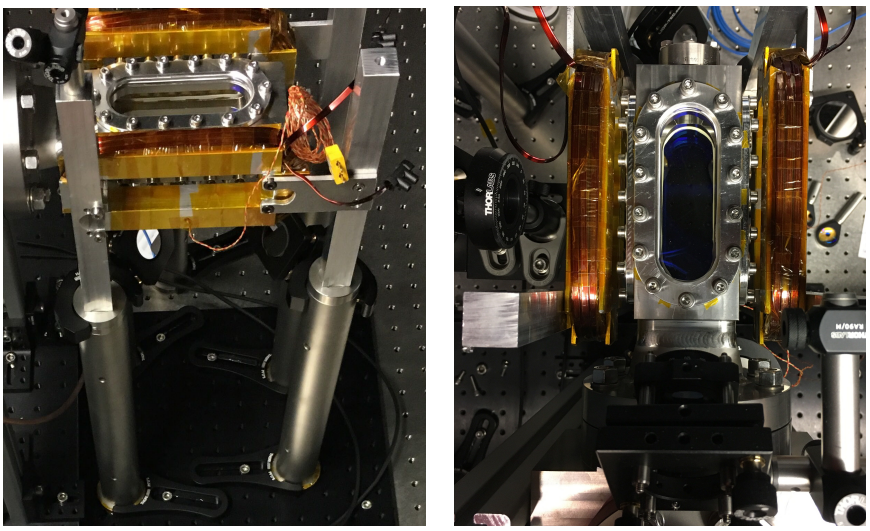

Figure 7.3: Side and top view of the MOT coils surrounding the science cell.

WINDING PROCESS The flat enamelled copper wire with dimensions 1 mm x 4 mm was wound onto the holder in three lanes with each lane containing 10 layers. After each row of flat copper wire we applied one layer of Kapton tape, which adds stability and thermal insulation.

Eddy currents

According to Faraday's law of induction, the magnetic field created by the copper coil induces a circulating current (i.e. eddy current) in the coil holder. This eddy current would then create a magnetic field that opposes the change in the original field. To avoid the generation of eddy currents in the holder, one of the connections between a short and a long side is blocked off with Kapton tape, stopping any current flow.

MOT COIL CHARACTERISTICS Table 7.1 summarizes the most relevant parameters of the MOT-coils, which are operated in anti-Helmholtz configuration. As the current running through the coils is of opposite direction, the fields created by the two coils counteract and thus lead to the required quadrupolar shape. For this coil configuration, the uniformity of the field gradient is optimized for $d = \sqrt{3}R$ (d: distance between the coils, R: effective radius of coils).

At a constant current of 20 A, the coils heat up to a maximum temperature of 80 °C. The distance between the coils is 77 mm, leaving only a 2 mm gap wrt. the science chamber (see figure 7.3). Increasing the distance would, however, diminish the uniformity of the gradient, as $d = \sqrt{3}R$ would not hold true anymore.

MOT gradient

Additionally, we measured the magnetic field at the operating current of 20 A in axial direction with a Gaussmeter, mounted onto a linear translation stage. The generated magnetic field is displayed in figure 7.4. The linear model fits well to the data, confirming the uniformity of the gradient in the center. The linear fit results in a magnetic field gradient of:

$$\nabla_z B = 15.07(1)\ \mathrm{G/cm}$$

Table 7.1: Summary of MOT coil parameters.

PARAMETER	VALUE	UNIT
Wire diameter	4 x 1	mm
Turns per coil	30	–
Operating current	20	A
Magnetic field gradient	15	G/cm
Resistance	290	mΩ
Inductance	220	μH
Maximum temperature	80	°C
Distance d between coils	77	mm

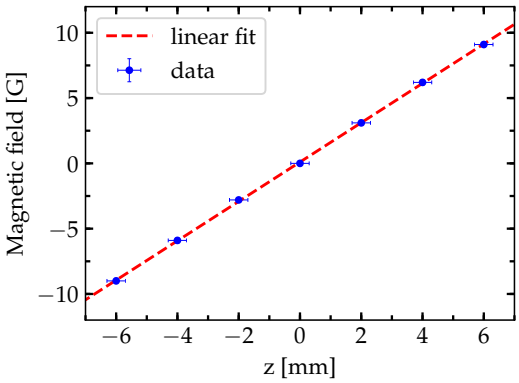

Figure 7.4: Magnetic field in the center between the two quadrupole coils at 20 A current. The linear behaviour exhibited by the data is confirmed by a linear fit.

In general $6 - 12$ G/cm are sufficient to achieve a MOT. Stronger gradients lead to a compression of the MOT, whereas smaller field gradients result in a shallower trap and a more dilute atomic cloud.

7.3 HUNT FOR THE K-MOT

After guiding the beams through the science cell and placing the MOT coils on either side of the cell, we tried to obtain the 3D MOT of ^{39}K. In the spirit of the 2D-MOT, we placed a CMOS-camera (MAKO G-030) with an objective in front of the science chamber. We positioned it facing the side of the chamber at a $\sim 45^\circ$ angle. Figure 7.5 shows an image, taken at this particular position, with the bright spots originating from the Z-beam. These spots are reflections off the input (left spot) and output window (right spot). The MOT should therefore appear exactly in the middle between these two spots, making it very easy to detect.

Having installed the probing system, we checked and tweaked a range of experimental parameters. First of all, we moved the whole

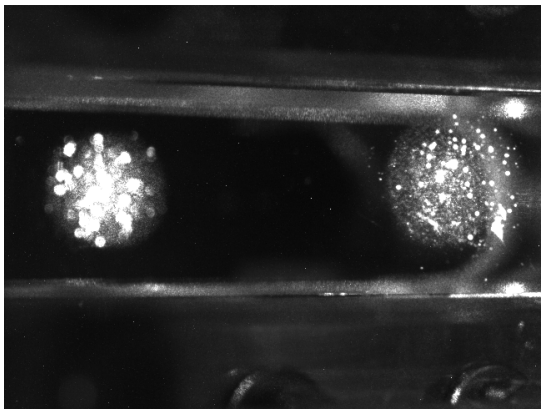

Figure 7.5: Side view of the science chamber with reflections of the Z-beam off the input (left) and output window (right).

vacuum system on the translation stage out of the magnetic coil contraption, to check the beam alignment. The six beams should cross at a single point $\mathbf{r}_0$. Furthermore, $\mathbf{r}_0$ should intersect with the magnetic field zero of the MOT coils, which was verified using the Gaussmeter. Once the vacuum system is returned to its original position, $\mathbf{r}_0$ should be in line of sight with the push beams from both 2D-MOT chambers.

Secondly, we checked the frequency and polarization of the MOT beams. Having the fluorescence in the 2D-MOT as a guideline and keeping in mind the individual detunings, we adjusted the respective AOM frequencies as well as the overall offset via the beat lock. The circularity of the beam polarizations was fine-tuned with the help of a polarimeter (*Schäfter + Kirchhoff* SK010PA-VIS).

Unfortunately, we were not able to detect a ^{39}K-MOT, as our experimental efforts were cut short by problems with the vacuum inside the chamber, which have not yet been resolved.

7.4 SUMMARY

In this chapter we presented the dual-species magneto-optical trap, which is loaded from the pre-cooled atoms from the two 2D-MOTs. Firstly, we expand the light from the laser table and then split it into three beams of equal intensity. The counter-propagating laser beams are realized in a retro-reflected arrangement. The magnetic field gradient, responsible for trapping, is created with a pair of coils in anti-Helmholtz configuration. Whilst hunting for the ^{39}K-MOT, we manually tuned different parameters in the experiment such as alignment, laser detuning and strength of the field gradient.

8

EXPERIMENTAL CONTROL SYSTEM

From the previous chapters we have learnt that we can control the frequency and intensity of laser beams via an AOM. Magnetic fields can be tuned by changing the current running though a pair of coils.These are just two examples of a wide variety of parameters that need tweaking in an experiment.

Up until now we had to manually turn each and every knob individually, for example when hunting for the ^{39}K MOT. However, in this chapter we will introduce a computer-based experimental control system, which can be interfaced with the different hardware devices.

The challenge in all of this is that, at a time resolution of a few 100 ns, sequences may last for up to a minute. These experimental sequences or shots can, for example, be comprised of linear voltage ramps or short pulses separated by some time delay. A computer-based control allows us to define a sequence and manipulate its parameters.

Guided by our experiences with the existing NaLi experiment [43], we decided to adapt the following approach:

- Analog output channels with 16-bit resolution. These outputs will be used, for example, for continuously tuning the frequency of a laser beam via an AOM.
- Digital TTL (3.3 V) outputs for switching devices such as shutters, that block a laser beam.
- Output channels should be terminated by BNC-adapters making them easily accessible.
- Reference oscillator, which ensures that the different channels are synchronised.
- Graphical User Interface (GUI) for defining and manipulating experimental parameters.
- Text-based interface for the experimental logic based on the Python programming language, which should be clear and easy to grasp.

Based on these ideas, we employed the software program *labscript suite* and chose the National Instruments (NI) hardware in accordance. After going through the most important features of the different hardware devices and how they interact with each other, the second part of this chapter focuses on how the sequences are initiated on the software side.

8.1 HARDWARE

The hardware (see figure 8.1 for an overview) used to control the experiment is based on the PXIe (acronym for PCI eXtensions for Instrumentation) bus system. The PXIe-system originates from the PCI-Bus system, which is the standard bus system for attaching hardware devices to computers, but also possesses synchronising features.

PXIe-chassis

The PXIe-chassis 1073 can house five cards and can be connected to the PC via an integrated controller. The PXI is interfaced with a remote PC via the host card NI PCI-8361, which is attached to the backpanel of the computer. A 100 MHz reference clock inside the chassis, translating to an update every 10 ns, synchronises the different cards. The cards in the chassis are routed on the backplane in a daisy-chain configuration, with each slot being connected to its neighbouring slot on the left and the right. Furthermore, each card has a separate clock, enabling their individual use. [43]

Pseudo-clock

However, we are using a software package, which requires the use of an external variable frequency master clock (i.e. pseudo-clock) to synchronise hardware devices. This makes it possible to step through hardware instructions only when an update is necessary. For example, when we want to have a constant output of 5 V for one minute, then we do not need to have an update every 10 ns. This ensures that the buffer does not get clogged up with redundant information. We are using the PulseBlasterUSB (*Spincore*), that features 24 output channels at 10 ns pulse resolution, as a pseudo-clock. The NI cards receive the triggering pulses from the PulseBlaster via their Programmable

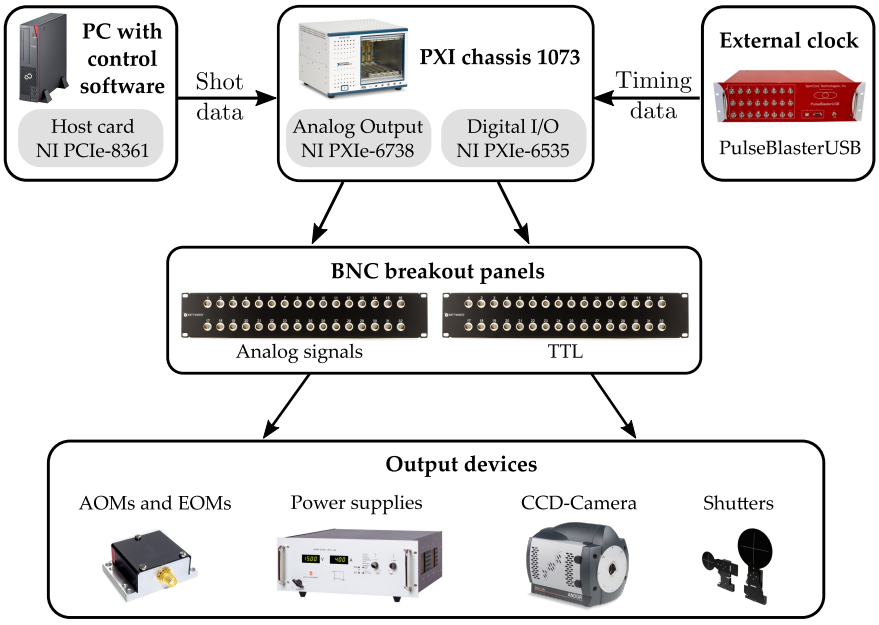

Figure 8.1: Overview of the hardware for the experimental control system. A PC controls the two NI cards, which are housed in a PXI chassis, via a host card. The cards are synchronised externally using an external clock.

Table 8.1: Specifications of the two NI cards we used for the computer-based experiment control. The update rate of the analog output module is given in mega-samples per second.

CARD	FEATURES
PXIe-6535	Digital I/O Module
	Number of data channels: 32
	Number of PFI channels: 6
	Clock rate: 10 MHz
	Maximum throughput: 40 MB/s
	Generation voltage: 3.3 V
	Buffer: 2048 samples
	Connector type: 68-pin VHDCI
PXIe-6738	Analog Output Module
	Number of data channels: 32
	Number of digital I/O channels: 10 (8 PFI)
	Resolution: 16 bit
	Maximum update rate: 1 MS/s
	Output range: $\pm$10 V
	Buffer: 65,535 samples
	Connector type: 68-pin SCSI

Function Input (PFI) channels.

Considering cost and corresponding features of the different available cards, we chose the NI-modules PXIe-6535 and PXIe-6738. The specifications of these two cards are summarized in table 8.1.

The digital I/O module PXIe-6535 is characterized by its 32 TTL channels at a clock rate of 10 MHz, while the analog output module PXIe-6738 features 32 analog signal channels with a 16-bit resolution.

In case a lot of channels are used at the same time, the sample rate gets reduced. Therefore samples can be temporarily stored in computer memory in a so-called buffer.

BNC breakout boards

The two NI cards have compact VHDCI- and SCSI-connectors to output the different analog and digital signals. In order to access all the outputs easily, efficiently and individually we are using self-assembled BNC breakout boards. These boards accept a VHDCI or SCSI connector as an input, split up the 68 connection lines and distribute them to the appropriate BNC-connectors. The digital I/O module with its VHDCI-connector has 38 BNC-outputs, while the analog module (SCSI-connector) houses 42.

The analog signals and TTL pulses can then be used to control e.g. AOMs, EOMs, power supplies, cameras or shutters.

8.2 THE LABSCRIPT SUITE

The hardware is interfaced with the *labscript suite* software developed by the Bose–Einstein condensate (BEC) research group at Monash University in Australia [44], which combines python-based experiment logic with a GUI for manipulating the experimental parameters. With a growing community around this software program, exchange of information, when facing problems, eases the implementation.

The experimental sequences or shots are defined via Hierarchical Data Format (HDF) files. These files allow the storage of large amounts of data. For every shot, a HDF-file is created and passed on between the different programs. These programs communicate with each other by writing to and reading from this file.

The working principle of labscript is illustrated in the flow diagram in figure 8.2 and can be summarized by the following steps:

1. `Shot preparation:` First you define parameters, that you want to tune and attribute some desired values in the **runmanager** application. The program will then create one HDF-file for each value. You can also give a list of values for each parameter. If there are multiple parameter lists, the program will perform a Cartesian product, ending up with all possible combinations.

   An application might be, for example, the optimization of the 3D MOT loading rate. Here, there are several parameters, such as laser detuning, laser power and magnetic field gradient, that need tweaking to identify the optimum.

   Once the parameter values have been added and the "Engage" button in the runmanager GUI has been pressed, labscript has to

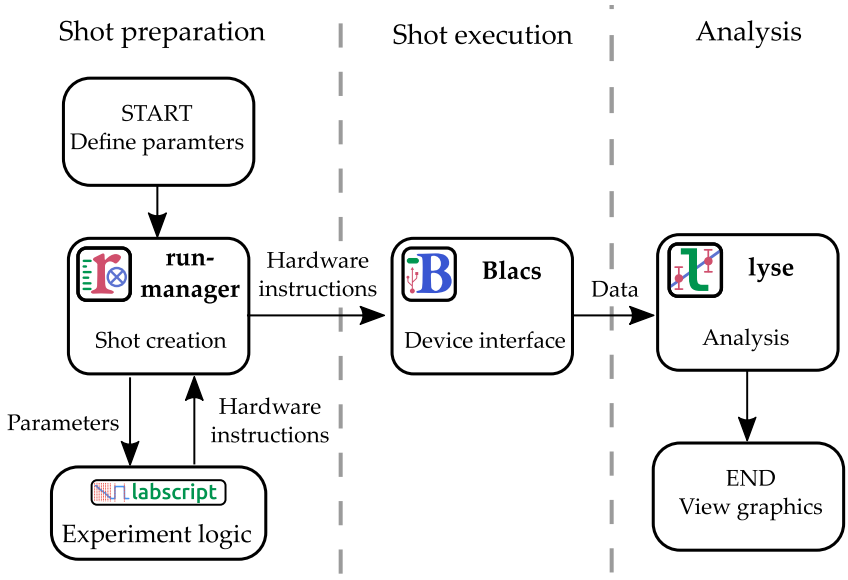

Figure 8.2: Flow diagram illustrating how the *labscript suite* functions: from preparing a shot, executing it through a hardware interface to finally analysing the acquired data (adapted from [44]).

translate the parameters into hardware instructions, which can be read in by the different devices. These instructions are then written into the HDF-file and this file is passed on to Blacs.

2. `Shot execution:` Each shot is executed by **Blacs**, as it interfaces with the connected devices. Firstly, the HDF-files are checked for compatibility with the corresponding hardware and then placed in a queue. Starting with the first shot, the program triggers the pseudo-clock and then continues under hardware timing.

3. `Analysis:` After each shot is executed, there is the possibility to send the acquired data to the analysis application **lyse**. Plots, created from user-written python scripts, can be produced for single or multiple shots.

8.3 SUMMARY

In this chapter we presented the experimental control system that allows us to program experimental sequences and eases the optimization process. The analog and digital output channels, which are synchronised by an external pseudo-clock, are controlled with the *labscript suite*. After the experimental parameters have been defined and manipulated via a graphical user interface, the software translates each sequence into instructions, which can be executed on the hardware.

9 CONCLUSION AND OUTLOOK

In this thesis we have reported on the design and setup of a new sodium potassium mixture experiment. The apparatus incorporates a versatile laser system, where we are able to switch between the two isotopes ^{39}K and ^{40}K. In combination with the bosonic ^{23}Na, this allows us to study both Boson-Boson and Boson-Fermion mixtures.

Furthermore, separate 2D MOT chambers for the two different atomic species, lead to a more modular setup allowing individual optimization. The 2D MOTs, which serve as a source of cold atoms for the dual species 3D MOT, feature a magnetic quadrupole field generated from permanent magnets. The magnetic field gradient in the 3D MOT, however, is produced by a pair of magnetic coils. At a current of 20 A the coils, which are operated in anti-Helmholtz configuration, yield a magnetic field gradient of ~ 15 G/cm.

Finally, we installed a experimental control system based on the *labscript suite* software program. Its 32 analog (16 bit) and 32 digital output channels allow us to automatize experimental sequences, which could last for up to a minute, at a time resolution of a few 100 ns.

The next steps in the experiment aim towards the realization of the dual species MOT. This will involve aligning the AOM paths on the sodium laser table and fixing the vacuum issues in the potassium 2D MOT chamber. Furthermore, a high resolution imaging system has to be set up, to determine the number of trapped atoms and their respective temperature. The experimental control system will allow for an efficient optimization of the MOT parameters, such as frequency detuning or magnetic field gradient.

After successfully cooling and trapping sodium and potassium atoms in the dual-species MOT, further steps towards quantum degeneracy have to be undertaken.

The overarching goal involves, therefore, the achievement of a ^{23}Na Bose-Einstein condensate in an optical dipole trap, as well as the implementation of optical tweezers for single K atoms. The immersion of tightly confined K atoms into a large cloud of Na atoms and the full control over both species, will allow us to perform experiments concerning dynamical gauge fields and the quantum heat engine.

A

TEMPERATURE CONTROL CIRCUIT

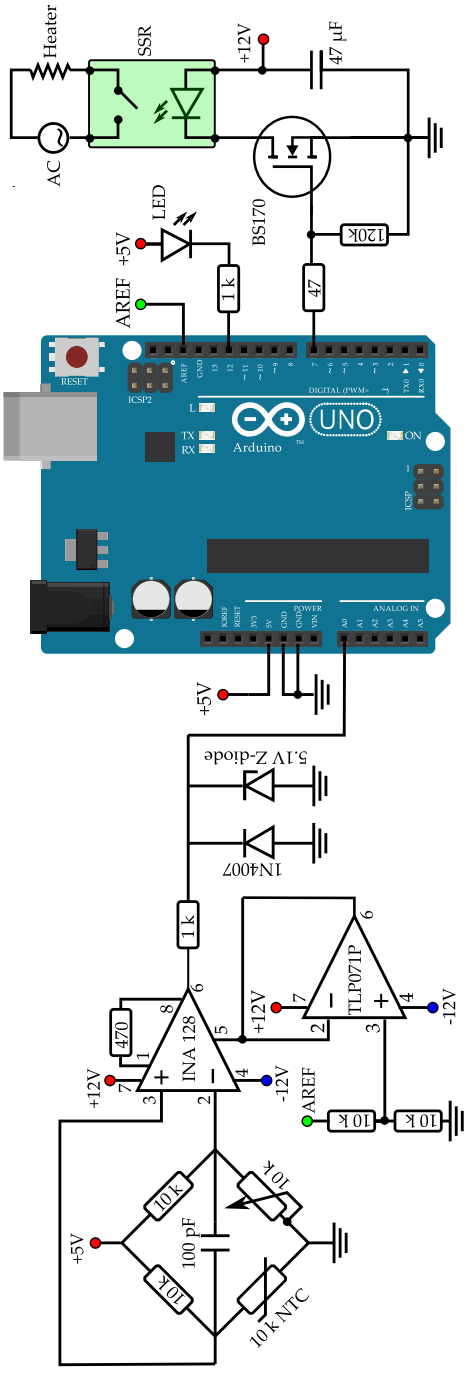

Figure A.1: Temperature control circuit for the potassium spectroscopy cell using a thermistor. The sensing circuit, comprising of a Wheatstone bridge, has been adapted from [45].

B

ENERGY LEVEL SCHEMES

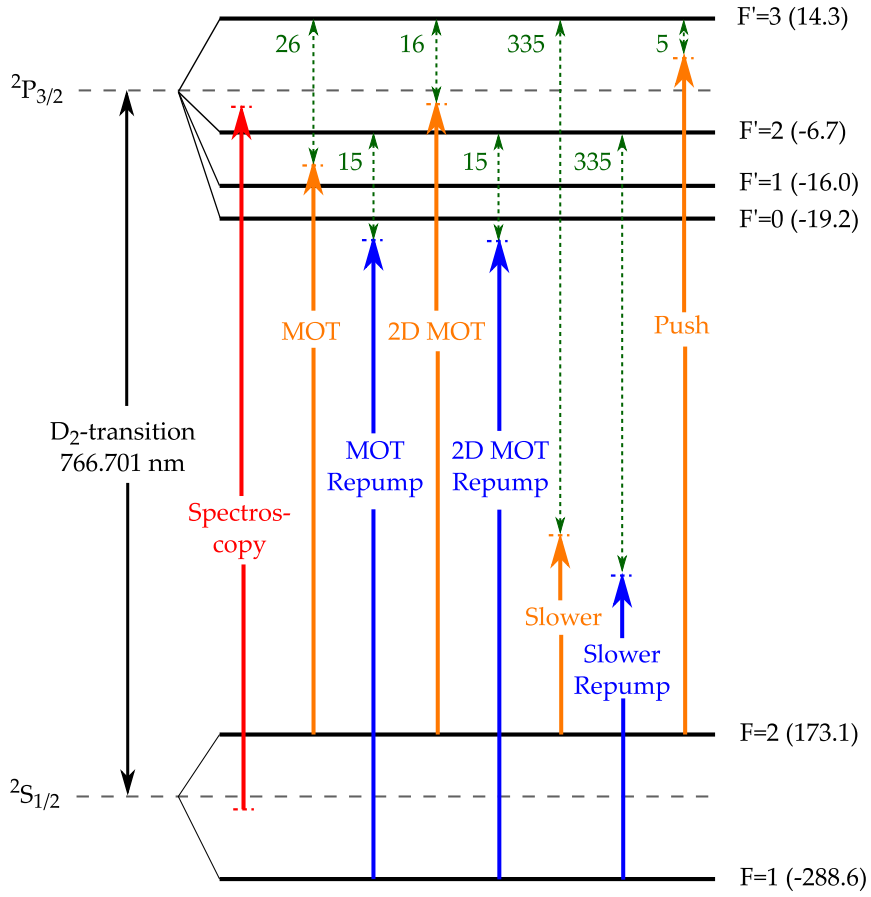

Figure B.1: Energy level scheme of ^{39}K with cooling (orange) and repumping (blue) transitions. The master laser is locked to the ground-state crossover (red line). The offset lock shifts slave lasers frequency by -410 MHz wrt. to the spectroscopy.

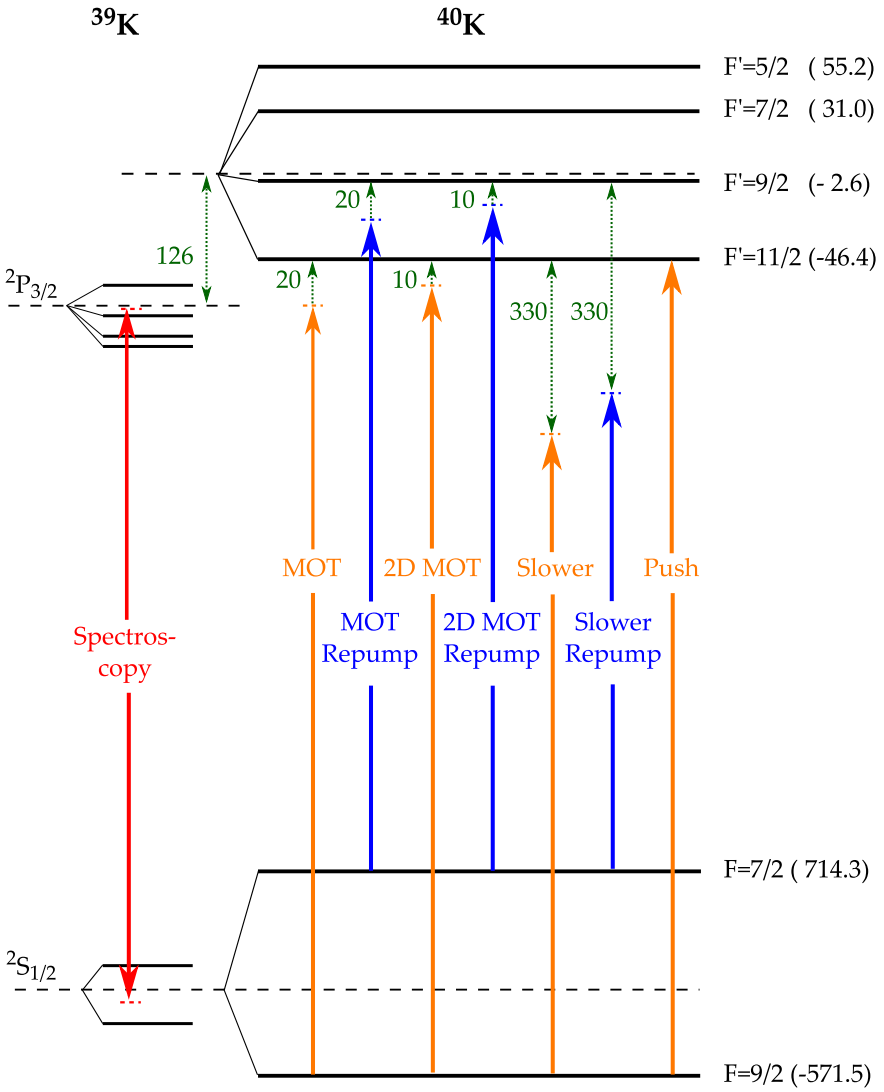

Figure B.2: Energy level scheme of ^{40}K with cooling (orange) and repumping (blue) transitions. The level scheme of ^{39}K is shown on the left for reference. The offset lock shifts slave lasers frequency by +406 MHz wrt. to the spectroscopy of ^{39}K.

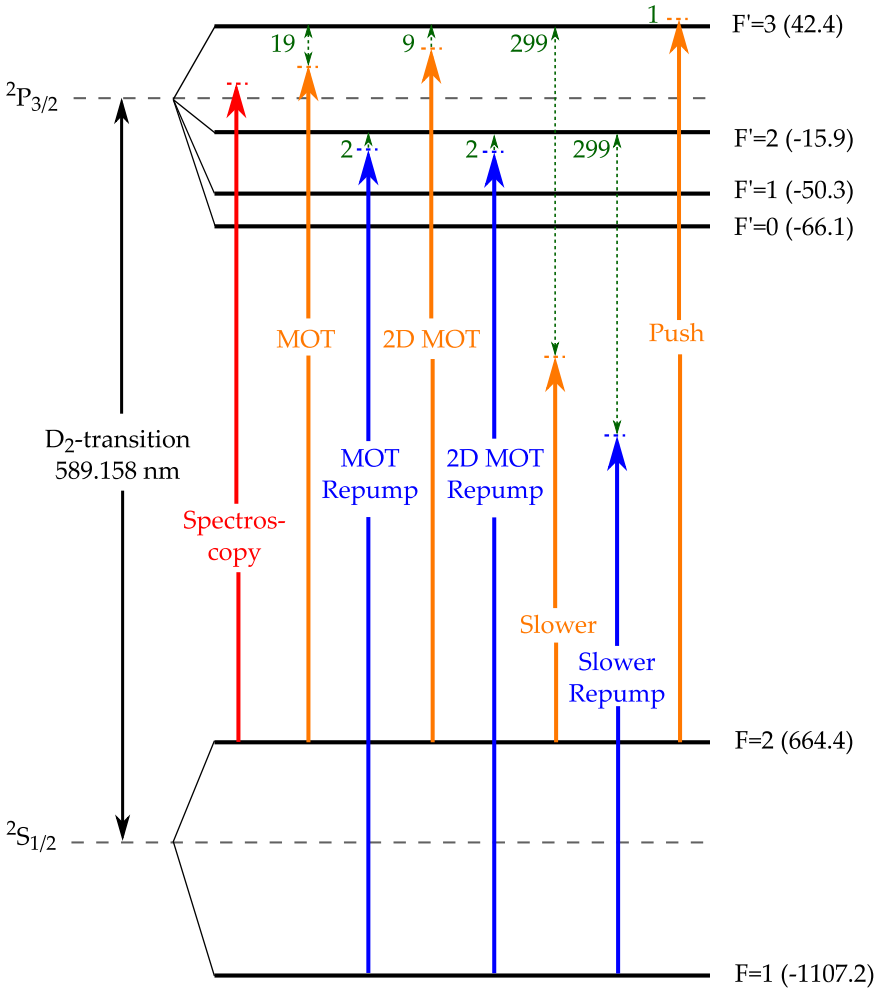

Figure B.3: Energy level scheme of ^{23}Na with cooling (orange) and repumping (blue) transitions. The light is stabilized to the excited-state crossover transition $F = 2 \rightarrow F' = 2, 3$.

LIST OF FIGURES

Figure 1.1 Schematic representation of the quantum heat engine. 1

Figure 1.2 Schematic illustration of the experimental implementation of dynamical gauge fields with ultracold atoms. 2

Figure 1.3 A Fermi sea of ^{40}K-atoms (blue) is coupled to a tightly confined, localized ^{23}Na-impurity (orange). 2

Figure 2.1 Doppler cooling configuration with the resulting velocity dependent scattering force. 6

Figure 2.2 MOT setup and energy diagram illustrating the working principle in one dimension. 7

Figure 3.1 3D view of the vacuum system. 10

Figure 3.2 Picture of the assembled vacuum apparatus from a bird's-eye view. 11

Figure 3.3 Images of the vacuum chambers on the main experimental table. 12

Figure 3.4 Differential pumping stage between the 2D MOT and the main chamber. 14

Figure 4.1 Vapour pressure of potassium and sodium as a function of temperature. 18

Figure 4.2 Energy level scheme for the D_2-line of ^{39}K, ^{40}K and ^{23}Na. 18

Figure 4.3 3D view of the spectroscopy cell encased in two brass cylinders with two heating bands attached on the outside. 20

Figure 4.4 Optical layout for saturated absorption spectroscopy. 21

Figure 4.5 Doppler-free absorption spectra of the D_2-line of potassium and sodium. 22

Figure 4.6 Model for frequency modulation spectroscopy, where the modulation of the laser frequency translates to an amplitude modulation, resulting in an error signal. 23

Figure 4.7 Error signals of potassium and sodium. 24

Figure 5.1 Side view of the two laser tables stacked on top of each other. 25

Figure 5.2 Overview of the optical layout on the potassium laser table, from which the different frequencies for cooling and trapping are produced. 26

Figure 5.3 Schematic of an ECDL in Littrow configuration. 26

Figure 5.4 Frequency offset lock scheme using a delay line. 27

Figure 5.5 Error signal of the potassium offset lock. 28

Figure 5.6 Sketch and image of a tapered amplifier diode. 29
Figure 5.7 Optical setup of the home-built fiberized TA module. 30
Figure 5.8 Characterization of the custom tapered amplifier module. 31
Figure 5.9 Theoretical principle and experimental usage of an acousto-optical modulator. 33
Figure 5.10 Schematic drawing of the optical layout on the potassium laser table for splitting and frequency-shifting the amplified laser light. 34
Figure 5.11 Cooling and repumping transitions of ^{39}K and ^{40}K (figure not to scale). 35
Figure 5.12 Schematic of the TA-SHG Pro (*TOPTICA Photonics*), which serves as our sodium laser. 37
Figure 5.13 Optical layout on the sodium laser table. 38
Figure 6.1 Schematic of the optical layout for the 2D MOT. 41
Figure 6.2 Measured magnetic field along the dipole moments direction for two magnets together with a model fit. 43
Figure 6.3 Schematic of the 2D-MOT magnetic field. 43
Figure 6.4 Numerical characterization of the 2D-MOT magnetic field. 44
Figure 6.5 Magnetic field along the propagation direction of one of the cooling beams. 45
Figure 6.6 Fluorescence in the potassium 2D-MOT. 46
Figure 7.1 Schematic of the optical layout for the 3D MOT. 47
Figure 7.2 3D schematic of the magnetic coils surrounding the science chamber. 48
Figure 7.3 Side and top view of the MOT coils surrounding the science cell. 49
Figure 7.4 Magnetic field in the center between the two quadrupole coils. 51
Figure 7.5 Side view of the science chamber with reflections of the Z-beam off the input and output windows. 51
Figure 8.1 Overview of the hardware for the experimental control system. 54
Figure 8.2 Flow diagram illustrating how the *labscript suite* functions: from preparing a shot, executing it through a hardware interface to finally analysing the acquired data. 56
Figure A.1 Temperature control circuit for the potassium spectroscopy cell using a thermistor. 61
Figure B.1 Energy level scheme of ^{39}K with cooling and repumping transitions. 63
Figure B.2 Energy level scheme of ^{40}K with cooling and repumping transitions. 64
Figure B.3 Energy level scheme of ^{23}Na with cooling and repumping transitions. 65

LIST OF TABLES

Table 4.1 Properties of natural potassium and sodium isotopes. 17

Table 5.1 Detunings and intensities of ^{39}K and ^{40}K laser beams. 36

Table 5.2 Projected detunings and powers of ^{23}Na laser beams. 39

Table 7.1 Summary of MOT coil parameters. 50

Table 8.1 Specifications of the two NI cards we used for the computer-based experiment control. 55

BIBLIOGRAPHY

[1] T.W. Hänsch and A.L. Schawlow. "Cooling of gases by laser radiation." In: *Optics Communications* 13.1 (1975), pp. 68 –69. ISSN: 0030-4018. DOI: https://doi.org/10.1016/0030-4018(75)90159-5. URL: http://www.sciencedirect.com/science/article/pii/0030401875901595.

[2] William D. Phillips. "Nobel Lecture: Laser cooling and trapping of neutral atoms." In: *Rev. Mod. Phys.* 70 (3 1998), pp. 721–741. DOI: 10.1103/RevModPhys.70.721. URL: https://link.aps.org/doi/10.1103/RevModPhys.70.721.

[3] F. Schreck, L. Khaykovich, K. L. Corwin, G. Ferrari, T. Bourdel, J. Cubizolles, and C. Salomon. "Quasipure Bose-Einstein Condensate Immersed in a Fermi Sea." In: *Phys. Rev. Lett.* 87 (8 2001), p. 080403. DOI: 10.1103/PhysRevLett.87.080403. URL: https://link.aps.org/doi/10.1103/PhysRevLett.87.080403.

[4] Andrew G. Truscott, Kevin E. Strecker, William I. McAlexander, Guthrie B. Partridge, and Randall G. Hulet. "Observation of Fermi Pressure in a Gas of Trapped Atoms." In: *Science* 291.5513 (2001), pp. 2570–2572. ISSN: 0036-8075. DOI: 10.1126/science.1059318. eprint: http://science.sciencemag.org/content/291/5513/2570.full.pdf. URL: http://science.sciencemag.org/content/291/5513/2570.

[5] M. H. Anderson, J. R. Ensher, M. R. Matthews, C. E. Wieman, and E. A. Cornell. "Observation of Bose-Einstein Condensation in a Dilute Atomic Vapor." In: *Science* 269.5221 (1995), pp. 198–201. ISSN: 0036-8075. DOI: 10.1126/science.269.5221.198. eprint: http://science.sciencemag.org/content/269/5221/198.full.pdf. URL: http://science.sciencemag.org/content/269/5221/198.

[6] K. B. Davis, M. O. Mewes, M. R. Andrews, N. J. van Druten, D. S. Durfee, D. M. Kurn, and W. Ketterle. "Bose-Einstein Condensation in a Gas of Sodium Atoms." In: *Phys. Rev. Lett.* 75 (22 1995), pp. 3969–3973. DOI: 10.1103/PhysRevLett.75.3969. URL: https://link.aps.org/doi/10.1103/PhysRevLett.75.3969.

[7] Richard P. Feynman. "Simulating physics with computers." In: *Int. J. Theor. Phys.* 21 (1982). [,923(1981)], pp. 467–488. DOI: 10.1007/BF02650179.

[8] Immanuel Bloch, Jean Dalibard, and Sylvain Nascimbène. "Quantum simulations with ultracold quantum gases." In: 2012.

[9] G. Modugno, G. Ferrari, G. Roati, R. J. Brecha, A. Simoni, and M. Inguscio. "Bose-Einstein Condensation of Potassium Atoms by Sympathetic Cooling." In: *Science* 294.5545 (2001), pp. 1320–1322. ISSN: 0036-8075. DOI: 10.1126/science.1066687. eprint: http://science.sciencemag.org/content/294/5545/1320.full.pdf.

URL: http://science.sciencemag.org/content/294/5545/1320.

[10] M. Mudrich, Stephan Kraft, K. Singer, Rudolf Grimm, Allard Mosk, and Matthias Weidemüller. "Sympathetic Cooling with Two Atomic Species in an Optical Trap." In: *Physical review letters* 88 (July 2002), p. 253001. DOI: 10.1103/PhysRevLett.88.253001.

[11] Wolfgang Niedenzu, Igor Mazets, Gershon Kurizki, and Fred Jendrzejewski. "Quantized refrigerator for an atomic cloud." In: *arXiv e-prints*, arXiv:1812.08474 (2018), arXiv:1812.08474. arXiv: 1812.08474 [quant-ph].

[12] Torsten Victor Zache, Florian Hebenstreit, Fred Jendrzejewski, M K. Oberthaler, Juergen Berges, and Philipp Hauke. "Quantum simulation of lattice gauge theories using Wilson fermions." In: *Quantum Science and Technology* 3 (Feb. 2018). DOI: 10.1088/2058-9565/aac33b.

[13] V Kasper, F Hebenstreit, F Jendrzejewski, M K Oberthaler, and J Berges. "Implementing quantum electrodynamics with ultracold atomic systems." In: *New Journal of Physics* 19.2 (2017), p. 023030. DOI: 10.1088/1367-2630/aa54e0. URL: https://doi.org/10.1088%2F1367-2630%2Faa54e0.

[14] Jun Kondo. "Resistance Minimum in Dilute Magnetic Alloys." In: *Progress of Theoretical Physics* 32.1 (July 1964), pp. 37–49. ISSN: 0033-068X. DOI: 10.1143/PTP.32.37. eprint: http://oup.prod.sis.lan/ptp/article-pdf/32/1/37/5193092/32-1-37.pdf. URL: https://dx.doi.org/10.1143/PTP.32.37.

[15] Fred Jendrzejewski. *Short notes on the Kondo effect and its potential realization in ultracold atomic gases*. URL: https://www.authorea.com/users/143341/articles/203821-short-notes-on-the-kondo-effect-and-its-potential-realization-in-ultracold-atomic-gases.

[16] Johannes Bauer, Christophe Salomon, and Eugene Demler. "Realizing a Kondo-Correlated State with Ultracold Atoms." In: *Phys. Rev. Lett.* 111 (21 2013), p. 215304. DOI: 10.1103/PhysRevLett.111.215304. URL: https://link.aps.org/doi/10.1103/PhysRevLett.111.215304.

[17] Cheng-Hsun Wu. "Strongly interacting quantum mixtures of ultracold atoms." PhD thesis. Massachusetts Institute of Technology, 2013. URL: http://hdl.handle.net/1721.1/83817.

[18] Zhenkai Lu. "Towards many body physics with ultracold NaK molecules." PhD thesis. LMU Munich, 2016.

[19] Nikolaus Walter Buchheim. "Dual-species apparatus for creating a dipolar quantum gas of 23Na40K molecules." PhD thesis. LMU Munich, 2015.

[20] Jee Woo Park, Cheng-Hsun Wu, Ibon Santiago, Tobias G. Tiecke, Sebastian Will, Peyman Ahmadi, and Martin W. Zwierlein. "Quantum degenerate Bose-Fermi mixture of chemically different atomic species with widely tunable interactions." In: *Phys. Rev. A* 85 (5 2012), p. 051602. DOI: 10.1103/PhysRevA.85.051602. URL: https://link.aps.org/doi/10.1103/PhysRevA.85.051602.

[21] Torben A. Schulze, Torsten Hartmann, Kai K. Voges, Matthias W. Gempel, Eberhard Tiemann, Alessandro Zenesini, and Silke Ospelkaus. "Feshbach spectroscopy and dual-species Bose-Einstein condensation of ^{23}Na$-^{39}$K mixtures." In: *Phys. Rev. A* 97 (2 2018), p. 023623. DOI: 10.1103/PhysRevA.97.023623. URL: https://link.aps.org/doi/10.1103/PhysRevA.97.023623.

[22] Min-Jie Zhu, Huan Yang, Lan Liu, De-Chao Zhang, Ya-Xiong Liu, Jue Nan, Jun Rui, Bo Zhao, Jian-Wei Pan, and Eberhard Tiemann. "Feshbach loss spectroscopy in an ultracold ^{23}Na $-^{40}$K mixture." In: *Phys. Rev. A* 96 (6 2017), p. 062705. DOI: 10.1103/PhysRevA.96.062705. URL: https://link.aps.org/doi/10.1103/PhysRevA.96.062705.

[23] C.J. Foot. *Atomic physics*. Oxford master series in physics. Oxford University Press, 2005. ISBN: 9780198506966.

[24] Peter van der Straten and Harold Metcalf. *Atoms and Molecules Interacting with Light: Atomic Physics for the Laser Era*. Cambridge University Press, 2016. DOI: 10.1017/CBO9781316106242.

[25] Julia Scherschligt, James A Fedchak, Daniel S Barker, Stephen Eckel, Nikolai Klimov, Constantinos Makrides, and Eite Tiesinga. "Development of a new UHV/XHV pressure standard (cold atom vacuum standard)." In: *Metrologia* 54.6 (2017), S125–S132. DOI: 10.1088/1681-7575/aa8a7b. URL: https://doi.org/10.1088%2F1681-7575%2Faa8a7b.

[26] D S. Barker, Eric Norrgard, N N. Klimov, James Fedchak, Julia Scherschligt, and S Eckel. *A single-beam Zeeman slower and magneto-optical trap using a nanofabricated grating*. Nov. 2018.

[27] Alexander Baumgärtner. "A new apparatus for trapping and manipulating single Strontium atoms." MA thesis. California Insitute of Technology, 2017.

[28] Giacomo Lamporesi, Simone Donadello, Simone Serafini, and G. Ferrari. "Compact high-flux source of cold sodium atoms." In: *The Review of scientific instruments* 84 (June 2013), p. 063102. DOI: 10.1063/1.4808375.

[29] John H Moore, Michael A Coplan, and Christopher C Davis. *Building scientific apparatus: a practical guide to design and construction*. London: Addison-Wesley, 1983. URL: https://cds.cern.ch/record/99961.

[30] Simone Donadello. "A compact high-flux source of cold sodium atoms." MA thesis. Università degli Studi di Trento, 2012.

[31] T.G. Tiecke. "Properties of Potassium." In: (2011). URL: http://www.tobiastiecke.nl/archive/PotassiumProperties.pdf.

[32] C. B. Alcock, V. P. Itkin, and M. K. Horrigan. "Vapour Pressure Equations for the Metallic Elements: 298–2500K." In: *Canadian Metallurgical Quarterly* 23 (July 1984), pp. 309–313. DOI: 10.1179/000844384795483058.

[33] A. Weis and S. Derler. "Doppler modulation and Zeeman modulation: laser frequency stabilization without direct frequency modulation." In: *Appl. Opt.* 27.13 (1988), pp. 2662–2665. DOI: 10.1364/AO.27.002662. URL: http://ao.osa.org/abstract.cfm?URI=ao-27-13-2662.

[34] Alexander Fabian Impertro. "Laser system for magneto-optical cooling and trapping of potassium." Bachelor thesis. University of Heidelberg, 2017.

[35] Thomas Uehlinger. "A 2D Magneto-Optical Trap as a High-Flux Source of Cold Potassium Atoms." Diploma thesis. ETH Zurich, 2008.

[36] Arno Trautmann. "Feshbach Spectroscopy of Sodium and Sodium-Lithium Mixtures." Diploma thesis. University of Heidelberg, 2011.

[37] Florian Volker Nicolai. "Design and construction of a fiber-coupled tapered amplifier system." MA thesis. University of Heidelberg, 2017.

[38] Alessandro Toffali. "Production of ultracold Sodium and Potassium atomic mixture in an optical dipole trap." MA thesis. Università degli Studi di Trento, 2013.

[39] E. A. Donley, T. P. Heavner, F. Levi, M. O. Tataw, and S. R. Jefferts. "Double-pass acousto-optic modulator system." In: *Review of Scientific Instruments - REV SCI INSTR* 76 (June 2005). DOI: 10.1063/1.1930095.

[40] T. G. Tiecke, S. D. Gensemer, A. Ludewig, and J. T. M. Walraven. "High-flux two-dimensional magneto-optical-trap source for cold lithium atoms." In: *Phys. Rev. A* 80 (1 2009), p. 013409. DOI: 10.1103/PhysRevA.80.013409. URL: https://link.aps.org/doi/10.1103/PhysRevA.80.013409.

[41] Patrícia Castilho, Edwin Pedrozo, E. M Gutierrez, P. Mazo, Giacomo Roati, Kilvia Farias, and V. Bagnato. "A compact experimental machine for studying tunable Bose–Bose superfluid mixtures." In: *Laser Physics Letters* 16 (Mar. 2019), p. 035501. DOI: 10.1088/1612-202X/ab00fb.

[42] Kai Henning Morgener. "Microscopy of 2D Fermi gases. Exploring excitations and thermodynamics." PhD thesis. Universität Hamburg, 2014.

[43] Jan Krieger. "Zeeman-Slower und Experimentsteuerung für das NaLi-Experiment." MA thesis. University of Heidelberg, 2008.

[44] Philip Starkey, Christopher Billington, S. P Johnstone, Martijn Jasperse, K. Helmerson, Lincoln Turner, and Russell Anderson. "A scripted control system for autonomous hardware-timed experiments." In: *Review of Scientific Instruments* 84 (Aug. 2013), p. 085111. DOI: 10.1063/1.4817213.

[45] Sören Bieling. "Design & Characterization of an Optical Filter Cavity." MA thesis. University of Heidelberg, 2015.

ACKNOWLEDGMENTS

An dieser Stelle möchte ich für ein tolles und lehrreiches Jahr Danke sagen:

- Fred, für die Möglichkeit dieses interessante und abwechslungsreiche Experiment mit aufzubauen. Durch dein außerordentliches Engagement und deine stets positive Art, war die Stimmung in der Gruppe immer ausgezeichnet.
- Selim Jochim, für die Übernahme der Zweitkorrektur.
- Lilo and Rohit. It was a lot of fun working with the two of you in the lab and discussing things in the office. I have learnt a lot from you over the past year. Thank you both for proof-reading this thesis.
- Andy. With your liveliness and positive craziness (i.e. andiness), there were no boring days in the lab or the office. I enjoyed the daily football discussions with you, as your analyses were (almost) always spot on.
- Apoorva, Alex, Kleiner Alex and the former group members Fabian, Kai and Kerim. You were always a great help in and around the lab. It was so much fun working alongside you.
- Danke an das gesamte SynQs-Team. Ihr habt uns in unserem Experiment in vielen Diskussionen durch eure experimentellen Erfahrungen enorm weitergeholfen.
- Herr Spiegel, Herr Martin-Almendrahl und Herr Azeroth. Danke für die Unterstützung und die Geduld beim Fräsen, bei unzähligen Bestellungen oder bei elektronischen Fragen und Problemen.
- Ein besonderer Dank geht an meine Eltern und Geschwister, die mich während des gesamten Studiums unterstützt haben.

DECLARATION

Ich versichere, dass ich diese Arbeit selbstständig verfasst und keine anderen als die angegebenen Quellen und Hilfsmittel benutzt habe.

Heidelberg, den 19. März 2019,

Jan Kilinc